On the evolution of an ice shelf melt channel at the base of Filchner Ice Shelf, from observations and viscoelastic modeling

Angelika Humbert[1,2], Julia Christmann[1], Hugh F. J. Corr[3], Veit Helm[1], Lea-Sophie Höyns[1,4], Coen Hofstede[1], Ralf Müller[5,6], Niklas Neckel[1], Keith W. Nicholls[3], Timm Schultz[5,6], Daniel Steinhage[1], Michael Wolovick[1], and Ole Zeising[1,2]

[1]Alfred-Wegener-Institut Helmholtz-Zentrum für Polar- und Meeresforschung, Bremerhaven, Germany
[2]University of Bremen, Department of Geosciences, Bremen, Germany
[3]British Antarctic Survey, Natural Environment Research Council, Cambridge, UK
[4]University of Bremen, Department of Mathematics and Computer Science, Bremen, Germany
[5]Institute of Applied Mechanics, University of Kaiserslautern, Kaiserslautern, Germany
[6]Division of Continuum Mechanics, Technical University of Darmstadt, Darmstadt, Germany

Correspondence: Angelika Humbert (angelika.humbert@awi.de)

Abstract. Ice shelves play a key role in the stability of the Antarctic Ice Sheet due to their buttressing effect. A loss of buttressing as a result of increased basal melting or ice shelf disintegration will lead to increased ice discharge. Some ice shelves exhibit channels at the base that are not yet fully understood. In this study, we present in-situ melt rates of a channel which is up to $330\,\mathrm{m}$ high and located in the southern Filchner Ice Shelf. Maximum observed melt rates are $2\,\mathrm{m\,a^{-1}}$. Melt
5   rates inside the channel decrease in the direction of ice flow and turn to freezing $\sim 55\,\mathrm{km}$ downstream of the grounding line. While closer to the grounding line melt rates are higher within the channel than outside, this relationship reverses further downstream. Comparing the modeled evolution of this channel under present-day climate conditions over 250 years with its present geometry reveals a mismatch. Melt rates twice as large as the present-day values are required to fit the observed geometry. In contrast, forcing the model with present-day melt rates results in a closure of the channel, which contradicts
10   observations. The ice shelf experiences strong tidal variability in vertical strain rates at the measured site and discrete pulses of increased melting occurred throughout the measurement period. The type of melt channel in this study diminishes in height with distance from the grounding line and are hence not a destabilizing factor for ice shelves.

1   Introduction

Melt channels carved upward into the base of ice shelves have been hypothesized to destabilize ice shelves and are often linked
15   to enhanced basal melt (Le Brocq et al., 2013; Langley et al., 2014; Drews, 2015; Marsh et al., 2016; Dow et al., 2018; Hofstede et al., 2021a). At some locations, these channels increase in height with distance from the grounding line, thus reducing the structural strength of the ice shelf, while at other locations they diminish downstream, minimizing their influence on shelf integrity. It remains unknown why some channels diminish downstream and whether channels that diminish downstream are also locations of enhanced basal melt.

Channels at the base of ice shelves may form where subglacial channels beneath the inland grounded ice discharge freshwater into the ocean (Le Brocq et al., 2013), or they may arise from topographic features or from shear margins developing surface troughs when adjusting to flotation (Alley et al., 2019). Features like bedrock undulations or eskers underneath the grounded ice may also leave a channel-like imprint in the geometry of the floating shelf (Drews et al., 2017; Jeofry et al., 2018). In all cases, the geometry of the channel at the ice base will be altered by two factors: incision due to basal melt arising from oceanic heat and closure due to viscoelastic creep.

Surface troughs on ice shelves are linked to incisions at the ice base, thus either to melt channels (e.g. Le Brocq et al., 2013; Langley et al., 2014) or to basal crevasses (e.g. Humbert et al., 2015). The surface troughs are formed by viscoelastic deformations in the transition to buoyancy and buoyancy equilibrium itself. Channels at the ice base have been surveyed using radio echo sounding (Rignot and Steffen, 2008; Vaughan et al., 2012; Le Brocq et al., 2013; Dutrieux et al., 2014; Langley et al., 2014; Dow et al., 2018). Their typical dimensions range from $300 - 500\,\mathrm{m}$ wide and up to $50\,\mathrm{m}$ high (Langley et al., 2014) to $1 - 3\,\mathrm{km}$ wide and $200 - 400\,\mathrm{m}$ high (Rignot and Steffen, 2008). Channel flanks are not necessarily smooth but may form terrace structures in the lateral (across ice flow) dimension as shown by Dutrieux et al. (2014) for Pine Island Glacier, Antarctica. These terraces are separated by up to $50\,\mathrm{m}$ high walls with steep slopes between $40°$ and $60°$.

Hofstede et al. (2021a) found a basal channel on Support Force Glacier at the transition to the Filchner Ice Shelf attributed to the outflow of subglacial water. The channel increases in height close to the grounding line and widens downstream. Between 7 and $14\,\mathrm{km}$ from the grounding line, the flanks of the channel become steeper and terraces form on its sides, which are sustained over $38\,\mathrm{km}$ from the grounding line, but with decreasing height between $14–38\,\mathrm{km}$. Within this distance, the height of the channel varies only slightly from 170 to $205\,\mathrm{m}$. This particular channel is the focus of this study.

Basal melt rates inside a channel underneath Ross Ice Shelf, Antarctica were found by Marsh et al. (2016) to be up to $22.2\,\mathrm{m\,a^{-1}}$ near the grounding line and only $2.5\,\mathrm{m\,a^{-1}}$ for observations $40\,\mathrm{km}$ downstream. Outside of the channel, the melt rate was only $0.82\,\mathrm{m\,a^{-1}}$ demonstrating enhanced melt inside the channel compared to its surroundings. At Pine Island Glacier, Antarctica, Stanton et al. (2013) found basal melt rates of up to $24\,\mathrm{m\,a^{-1}}$ and an across-channel variability that they suggested to be related to channelized flow. The decrease of channel melt rates with distance downstream is likewise described by Le Brocq et al. (2013). Buoyant freshwater initially enhances basal melting inside the channel by increasing the vigor of the turbulent plume at the ice base and entraining more ambient warm water (Jenkins and Doake, 1991). However, at some point the rising plume can become super-cooled due to the falling pressure, which leads to the formation of frazil ice and freeze-on. This is a general feature of the thermohaline circulation underneath ice shelves (e.g. MacAyeal, 1984). Similar to Le Brocq et al. (2013), Marsh et al. (2016) assumed that the channel at Ross Ice Shelf is formed by the outflow of subglacial meltwater. Washam et al. (2019) found high seasonal variability in basal melting within a channel at Petermann Gletscher, Greenland. In summer, melt rates reached a maximum of $80\,\mathrm{m\,a^{-1}}$, whereas in winter, melt rates were below $5\,\mathrm{m\,a^{-1}}$. They suggested that increased subglacial discharge during summer strengthens ocean currents under the ice, which drives the high melt rates. Besides seasonal variability, melt rates also change within smaller periods. Vaňková et al. (2020) identified melt rate variations at the semi-diurnal M_2 tidal constituent at six of 17 locations at Filchner-Ronne Ice Shelf, Antarctica. Likewise, Lindbäck et al. (2019) and Sun et al. (2019) found diurnal and fortnightly melt variations at other Antarctica ice shelves. In-situ observations of

55   melt rates in sub-ice-shelf channels are often conducted with a phase sensitive Radio Echo Sounder (pRES), which is described in more detail below.

Modeling basal melt rates adequately requires fully coupled ice-ocean models, that evaluate the energy balance at the ice-ocean transition to compute basal melt rates. While none of the global circulation models deals with ice shelf cavities, there are some coupled ice-sheet-ocean models simulating large scale basal melt rates (Gwyther et al., 2020; Dinniman et al., 2016;

60   Jourdain et al., 2017; Seroussi et al., 2017; Timmermann and Hellmer, 2013; Galton-Fenzi et al., 2012). However, only a few of them incorporate melt channels as this requires very high horizontal resolution: Gladish et al. (2012) showed that channels confine the warm water and stabilize the ice shelf by preventing melt on broader spatial scales. This conclusion is affirmed by Millgate et al. (2013) who found that an increasing number of melt channels lead to a decreasing overall mean melt rate. Our study will provide an observational dataset of basal melt rates that allows understanding these types of modeling results.

65   The change in geometry due to mechanical deformation is another important contribution to the evolution of basal channels (Bassis and Ma, 2015; Wearing et al., 2021). The spatial gradients in displacement u lead to strain ε that causes a change in ice thickness. This process is governed by the viscoelastic nature of a Maxwell fluid for ice. While ice is reacting purely viscously on long time scales, its behavior on short time scales is elastic (Reeh et al., 2000; Gudmundsson, 2011; Sergienko, 2013; Humbert et al., 2015; Christmann et al., 2016; Schultz, 2017; Christmann et al., 2019). The transition from grounded

70   to floating ice and short term geometry changes due to basal melt or accumulation are examples of ice affected by the elastic response. Over time scales of years, viscous creep becomes more relevant. As a consequence, the geometry of melt channels needs to be modeled using viscoelastic material models based on a characteristic Maxwell time of $153\,\mathrm{d}$ (deduced in the model section) arising from the material parameters used for this study. Until now, the viscoelastic nature of the evolution of basal channels was neglected as previous studies only consider viscous ice flow.

75   In this study, we present in-situ melt rates of a large melt channel feature in the southern Filchner Ice Shelf at the inflow from Support Force Glacier (SFG). Field measurements and satellite-borne data provide constraints to investigate how this feature evolves using numerical modeling. In addition to the spatial distribution of basal melt, we analyze the temporal evolution of melt rates. We split this manuscript into two main parts, starting with observations followed by a modeling section. We present the methodology and the results in each part separately. A synthesis then follows focusing on the evolution of the melt channel.

80   2   Observations

2.1   Data acquisition

We acquired data at a melt channel on the southern Filchner Ice Shelf under the framework of the Filchner Ice Shelf Project (FISP). We performed 44 phase-sensitive radar (pRES) measurements (locations are shown in Fig. 1) in the season 2015/16, that have been repeated in 2016/17 as Lagrangian-type measurements. These measurements were taken in 13 cross-sections

85   ranging from 14 to $61\,\mathrm{km}$ downstream from the grounding line (Fig. 1). This allows us to investigate the spatial variability of basal melt rates. At each cross-section, up to four measurements were performed at different locations: at the steepest western flank (SW), at the lowest surface elevation (L), at the steepest eastern flank (SE) and outside east of the channel (OE; Fig. 1b).
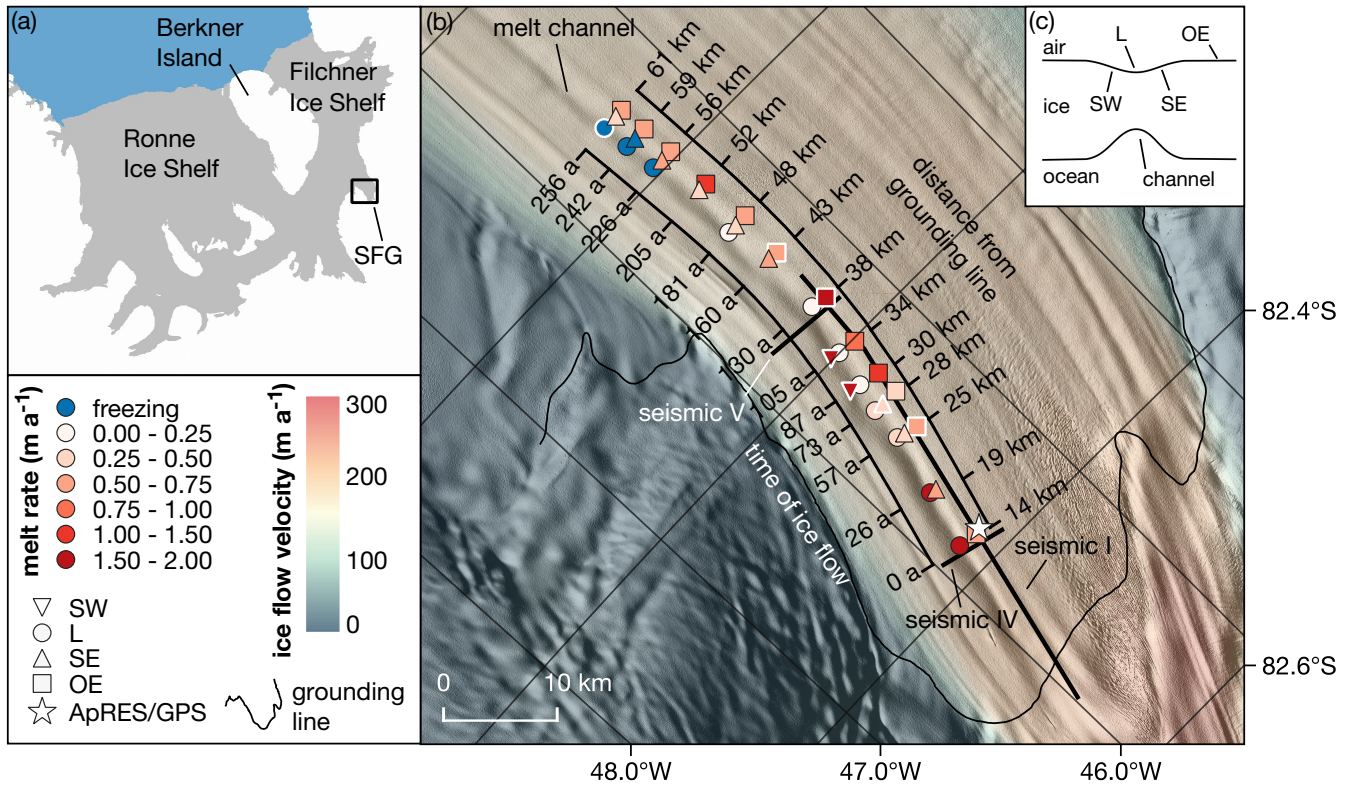
Figure 1. (a) Map of the Ronne and Filchner ice shelves. The study area near the Support Force Glacier (SFG) is marked with a black box. (b) Study area with pRES-derived basal melt rates at 13 cross-sections of the melt channel. The different symbols indicate the position relative to the channel, as shown in (c). Those melt rates derived from a nadir and an off-nadir basal return are marked with a white outline. For each cross-section, the distance from the grounding line and the duration of ice flow from the location furthest upstream are given. The location of an ApRES/GPS station is shown by a star. The seismic I, IV and V lines mark the location of active seismic profiles (Hofstede et al., 2021a, b). The background is a hillshade of the Reference Elevation Model of Antarctica (Howat et al., 2018, 2019) overlaid by the ice flow velocity (Hofstede et al., 2021a). (c) Sketch of a cross-section of the channel with measurement locations on the steepest western surface flank (SW), at the lowest surface elevation (L), on the steepest eastern surface flank (SE) and outside east of the channel (OE).

In order to achieve an all-year time series, one autonomous pRES (ApRES) station was installed (Fig. 1b). This instrument performed autonomous measurements every two hours resulting in 4342 measurements between 10 January 2017 and 6 January 2018. One year earlier, a GPS station was also in operation at this point from December 24, 2015 to May 5, 2016, the data of which we use for tidal analysis. To distinguish the single-repeated measurements from the autonomous measurements, we refer to them as *pRES* and *ApRES* measurements, respectively.

90

2.2 Materials and methods

2.2.1 pRES device and processing

The pRES device is a low-power, ground-based radar that allows for estimating displacement of layers from repeated measurements with a precision of millimeters (Brennan et al., 2014). This accuracy enables the investigation of even small basal melt rates, taking into account snow accumulation together with firn compaction and strain in the vertical direction (Corr et al., 2002; Jenkins et al., 2006). The pRES is a frequency modulated continuous wave (FMCW) radar that transmits a sweep, called *chirp*, over a period of one second with a center frequency of $300\,\mathrm{MHz}$ and bandwidth of $200\,\mathrm{MHz}$ (Nicholls et al., 2015). For a better signal to noise ratio, the single-repeated measurements were performed with 100 chirps per measurement and the measurements of the time series with 20 chirps due to memory and power limitations. After collecting the data, anomalous chirps within each burst were removed and the remaining chirps were stacked. Anomalous chirps were identified by correlating each chirp with every other chirp of the burst. Those with a low correlation coefficient on average were rejected.

We followed Brennan et al. (2014) and Stewart et al. (2019) for data processing to get amplitude- and phase-depth profiles. The final profile that contains the amplitude and phase information as a function of two-way travel time was obtained from a Fourier transformation. To convert two-way travel time into depth, the propagation velocity of the radar wave is computed following Kovacs et al. (1995). For this the vertical ice/firn density profile is required. Here we use a model described by Herron and Langway (1980). As input parameters, accumulation rate and mean annual temperature are needed, for which we use data from the regional climate model RACMO 2.3/ANT (van Wessem et al., 2014, multi-annual mean 1979 – 2011). Despite the correction of higher propagation velocities in the firn, the uncertainty of the velocity and thus of the depth is 1% (Fujita et al., 2000).

2.2.2 Basal melt rates from repeated pRES measurements

The method for determining basal melting rates, previously described by e.g. Nicholls et al. (2015) and Stewart et al. (2019), is based on the ice thickness evolution equation. The change in ice thickness over time $\partial H / \partial t$ consists of components arising from deformation and accumulation/ablation at both interfaces (e.g. Zeising and Humbert, 2021). As our observations are discrete in time, the change of ice shelf thickness ΔH within the time period Δt, that is caused by changes at the surface and in the firn ΔH_s (e.g. snow accumulation/ablation and firn compaction), by strain in vertical direction ΔH_ε and by thickness changes due to basal melt ΔH_b is considered:

$$\frac{\Delta H}{\Delta t} = \frac{\Delta H_s}{\Delta t} + \frac{\Delta H_\varepsilon}{\Delta t} + \frac{\Delta H_b}{\Delta t} \tag{1}$$

(Vaňková et al., 2020; Zeising and Humbert, 2021). In order to obtain the basal melt rate, the change in ice thickness must be adjusted for the other contributions. Snow accumulation/ablation, firn compaction but also changes in radar hardware or settings (a different pRES instrument was used for the revisit) can cause a vertical offset near the surface that cannot be distinguished from one another. Following Jenkins et al. (2006), we aligned both measurements below the firn-ice transition. To this end, we computed the depth of pore closure h_{pc} takes place, i.e. the depth at which a density of $830\,\mathrm{kg\,m^{-3}}$ is reached.

125 We apply the densification model (Herron and Langway, 1980) and mean annual accumulation rate and temperature from the multi-year mean RACMO2.3 product (van Wessem et al., 2014). In our study area, h_{pc} varies between $62\,\mathrm{m}$ and $71\,\mathrm{m}$. The actual alignment is based on a correlation of the amplitudes for a window of $6\,\mathrm{m}$ around h_{pc}. No reliable alignment could be obtained from the correlation for nine stations because the correlations of the surrounding depths resulted in ambiguous alignments. As a consequence, these stations were not considered.

130 After the alignment, the change in the ice thickness H_i below the pore closure depth h_{pc} is only affected by vertical strain and basal melt. Thus the basal melt rate a_b (positive for melting, negative for freezing) is

$$a_b = -\frac{\Delta H_b}{\Delta t} = -\left(\frac{\Delta H_i}{\Delta t} - \frac{\Delta H_\varepsilon}{\Delta t} \right) \tag{2}$$

with ΔH_ε being the thickness change due to vertical strain $\varepsilon_{zz}^{\mathrm{obs}}$. ΔH_ε is derived from integrating $\varepsilon_{zz}^{\mathrm{obs}}$ from the aligned reflector at h_{pc} to the ice base h_b

$$135 \quad \Delta H_\varepsilon = \int_{\overline{h_b}}^{h_{\mathrm{pc}}} \varepsilon_{zz}^{\mathrm{obs}}\,\mathrm{d}z. \tag{3}$$

Here, $\overline{h_b}$ denotes the average depth of the ice base of the measurements. The vertical strain is defined as

$$\varepsilon_{zz}^{\mathrm{obs}} = \frac{\partial u_z}{\partial z} \tag{4}$$

with the displacement in vertical direction u_z.

In order to determine u_z, we followed the method described by Stewart et al. (2019). We divided the first measurement in
140 segments of $6\,\mathrm{m}$ width with $3\,\mathrm{m}$ overlap from a depth of $20\,\mathrm{m}$ below the surface to $20\,\mathrm{m}$ above the ice base. To determine vertical displacements, we cross-correlated each segment of the first measurement with the repeated measurement. The lag of the largest amplitude correlation coefficient was used to find the correct minimum phase difference, from which we derived the vertical displacement. Since noise prevents the reliable estimation of the vertical displacement from a certain depth on, we calculated the depth at which the averaged correlation of unstacked chirps undercuts the empirical value of 0.65. We name this
145 the noise-level depth limit h_{nl}, which is $743\,\mathrm{m}$ on average in this study area. Only those segments located below h_{pc} and above h_{nl} were used to avoid densification processes and noise to influence the strain estimation. A linear regression was calculated from the shifts of the remaining segments, assuming a constant vertical strain distribution over depth as the overall trend. However, at six stations, all in the hinge zone where the ice is bent by tides, we observed a slight deviation from a linear trend at deeper layers (Fig. A1a). A depth-dependent tidal vertical strain caused by tidal bending near the grounding line has been
150 observed previously (Jenkins et al., 2006; Vaňková et al., 2020) although the long-term vertical strain was found to be depth independent (Vaňková et al., 2020). The segments that indicate a non-linear distribution are located below h_{nl} and are hence not taken into account for the regression. Nevertheless, we want to provide a lower limit of $|\Delta H_\varepsilon|$ considering other forms of strain-depth relations (Jenkins et al., 2006). For this purpose, we use a strain model that is decreasing linearly from half the ice

thickness (approximately h_{nl}) to the depth of at which $\varepsilon_{zz}^{\mathrm{obs}} = 0$ (Fig. A1b). This serves as a lower limit of $|\Delta H_\varepsilon|$, whereas a linear $\varepsilon_{zz}^{\mathrm{obs}}(z)$ gives the upper limit. The average of both gives ΔH_ε and the difference the uncertainty.

In order to derive ΔH_i, we used a wider segment of $10\,\mathrm{m}$ around the basal return, which was identified by a strong increase in amplitude. Its upper limit is located $9\,\mathrm{m}$ above the basal return, while the lower limit is defined $1\,\mathrm{m}$ below the basal return. The vertical displacement of the ice base and thus the change in ice thickness was obtained from the cross-correlation of the basal segment. However, more than one strong basal reflection occurred at 7 sites. For these sites, we averaged the melt rates we derived from both basal segments. In Appendix A1 we discuss the identification of the basal reflection and the influence of off-nadir basal returns on the estimation of basal melt rates (Tab. A1, Figs. A2 and A3).

The uncertainty of the melt rate results mainly from the alignment of the repeated measurement and the uncertainty of ΔH_ε. This leads to uncertainties in the melt rate of up to $0.26\,\mathrm{m\,a^{-1}}$ for locations in the hinge zone, while at other locations the uncertainty is predominantly in the range of $< 0.05\,\mathrm{m\,a^{-1}}$. At those stations where the melt rate was averaged, the error represents the difference of the two melt rates. Since this difference is up to $1.34\,\mathrm{m\,a^{-1}}$, the error significantly exceeds $0.26\,\mathrm{m\,a^{-1}}$ in some cases.

2.2.3 Benchmarking melt rates and thickness evolution

In order to classify how representative the melt rates are for the past, we reconstructed the ice thickness based on the values derived from the pRES measurements. First, we linearly interpolated a_b, ΔH_ε and ΔH_s along the distance of the channel to get continuous values between the cross-sections and smoothed the results in order to obtain a trend for each process. We converted the distance from the upstream-most cross-section to an age beyond this cross-section by assuming the mean flow velocity is constant in time and space. Next, we treat the change in ice thickness as a transport equation. To this end, we compute the advection of the ice thickness along the flowline under present day climate conditions (H_{PDadv}). For this we use interpolated functions of $a_b(t)$, $\Delta H_\varepsilon(t)$ and $\Delta H_s(t)$. The expected ice thickness at H_{PDadv} is then the thickness at $t_0 = 0\,\mathrm{a}$ plus the cumulative change in ice thickness:

$$H_{\mathrm{PDadv}}(t) = H(t_0) + \int_{t_0}^{t} \left(\Delta H_s(t') + \Delta H_\varepsilon(t') + a_b(t') \right) dt'. \tag{5}$$

We can invert this and calculate a synthetic melt rate $a_b^{\mathrm{syn}}(t)$ that reconstructs the observed ice thickness H:

$$H(t) = H(t_0) + \int_{t_0}^{t} \left(\Delta H_s(t') + \Delta H_\varepsilon(t') + a_b^{\mathrm{syn}}(t') \right) dt'. \tag{6}$$

Descriptions of the symbols are given in Tab. A2.

2.2.4 Basal melting from ApRES time series

The processing of the autonomous measured time series with a 2-hour measurement interval differs slightly from the single-repeated measurements. For the ApRES time series, the instrument was located below the surface, thus snow accumulation had

no influence on the measured ice thickness and an alignment of the measurements is not necessary. This gives the possibility to determine the firn compaction ΔH_f. Without the alignment, thickness change due to strain needs to be considered for the whole ice thickness H

$$\Delta H_\varepsilon = \int_0^H \varepsilon_{zz}^{\text{obs}} \, \mathrm{d}z. \tag{7}$$

For processing, we followed the method described by Zeising and Humbert (2021), which differs slightly from the processing applied by Vaňková et al. (2020). Similar to processing of the single-repeated measurements, we divided the first measurement into the same segments and calculated the cross-correlation of the first measurement (t_1) with each repeated measurement (t_i). The displacement was obtained by the lag of the minimum phase difference. To avoid half-wavelength ambiguity due to phase wrapping, we limited the range of expected lag based on the displacement derived for the period $t_1 - t_{i-1}$.

The estimation of the vertical strain for the period $t_1 - t_i$ is based on a regression analysis of the vertical displacements for chosen segments. Only those segments located below a depth of $70\,\mathrm{m}$ and above the noise-level depth limit of $h \approx 600\,\mathrm{m}$ were used to avoid densification processes and noise influencing the strain estimation. Assuming constant strain over depth, the regression analysis gives the vertical strain and the cumulative displacement $u_z(z)$ is

$$u_z(z) = \varepsilon_{zz}^{\text{obs}} z + \Delta H_f \tag{8}$$

where the intercept at the surface is the firn compaction ΔH_f. Similar to determination of ΔH_i of the single-repeated measurements, we derived the change in ice thickness ΔH for a wider segment of $10\,\mathrm{m}$. The cumulative melt of the ApRES time series was finally derived by

$$\Delta H_b(t) = -\int_{t_1}^t \left(\Delta H(t') - \Delta H_\varepsilon(t') - \Delta H_f(t') \right) dt'. \tag{9}$$

In order to investigate if the basal melt is affected by tides, we first de-trended the cumulative melt time series and computed the frequency spectrum afterwards.

Subsequently, we used the time series of $\Delta H(t)$ to investigate the occurrence of non-tidal melt events. We de-tided $\Delta H(t)$ twice, once by subtracting a harmonic fit based on frequencies up to the fortnightly constituent (Mf) and secondly up to the solar annual constituent (Sa) to remove all tidal induced signals and to calculated the thinning rate afterwards. In this way, we identify non-tidal melt events and the influence of annual/seasonal signals without estimating the correct amount of strain thinning/thickening. Assuming that basal melt causes changes on short time scales of several days, we attribute abrupt increases in the thinning rate to basal melt anomalies.

2.2.5 Global Positioning System (GPS) processing

The GPS processing is similar to the method used by Christmann et al. (2021). With the Waypoint GravNav 8.8 processing software, we applied a kinematic precise point positioning (PPP) processing for the GPS data that were stored in daily files.

We merged three successive daily solutions to enable full day overlaps avoiding jumps between individual files. Afterwards, we combined the files in the middle of each 1-day overlap using relative point to point distances and removed outliers. The data has been low-pass filtered for frequencies higher than $1/3600\,\mathrm{Hz}$. For tidal analysis, we calculated the power spectrum of the vertical displacement.

2.2.6 Digital Elevation Model (DEM)

We use the TanDEM-X PolarDEM 90m Digital Elevation data product provided by the German Aerospace Center (DLR) as reference elevation model (DLR, 2020). As the elevation values represent ellipsoidal heights relative to the WGS84 ellipsoid we refer the PolarDEM to the EIGEN-6C4 Geoid (Foerste et al., 2014). In the following, we refer the DEM heights above Geoid as observed surface elevation h_{TDX}. The absolute vertical height accuracy of the PolarDEM is validated against ICESat data and given to be $< 10\,\mathrm{m}$ (Rizzoli et al., 2017). For our region of interest the accuracy is given to be $< 5\,\mathrm{m}$ as shown in Fig. 16 of Rizzoli et al. (2017).

2.3 Results and discussion of observations

2.3.1 Spatial melt rate distribution around basal channel

We were able to determine basal melt rates at 34 of the 44 single-repeated pRES measurements. At some of the excluded stations, low correlation values prevented the alignment at the firn-ice transition or the estimation of the vertical strain. At others, a change in the shape of the first basal return prevented the determination of the change in ice thickness.

The estimated basal melt rates range from 0 to $2\,\mathrm{m\,a^{-1}}$, with the largest melt rates on the steepest western flank (SW) of the channel (Fig. 2a). A trend of decreasing melt rates in the along channel direction was found at the highest part (L) of the channel. Here, melt rates decrease from $1.8\,\mathrm{m\,a^{-1}}$ to basal freezing, measured at the three most downstream cross-sections. Outside of the channel (OE), basal melt rates are more variable without a trend. Stations at the eastern flank (SE) show a lower range of variability. Here, a_b varies between basal freezing and $0.8\,\mathrm{m\,a^{-1}}$.

The height of the channel (difference in ice thickness between L and OE; Fig. 2b) increases from about $200\,\mathrm{m}$ at the southernmost cross-section to a maximum of about $330\,\mathrm{m}$ over a distance of $20\,\mathrm{km}$ in ice flow direction. At this location the melt rates within the channel fall below those outside the channel and the height of the channel decreases, reaching $\sim 100\,\mathrm{m}$ at the northernmost cross-section.

In Fig. 2c we display the melt rates as a function of ice-shelf draft, derived from the TanDEM-X surface elevation and the pRES ice thickness. The melt rates outside the channel (OE) seem to be independent of the ice-shelf draft, while inside the channel (L) the melt rates decrease with reduced draft. However, melt rates at the largest draft inside the channel are approx. three times larger than those outside the channel or at the steepest eastern flank (SE) at similar draft.

The distribution of ΔH_ε shows a significant thickening of more than $1\,\mathrm{m\,a^{-1}}$ at the most upstream cross-section at L and OE (Fig. A4). In the ice flow direction, ΔH_ε declines, reaching about zero above the channel at the cross-section furthest

245   downstream. In contrast, outside the channel, strain-thinning occurred from $30\,\mathrm{km}$ downstream the grounding line. The change in ice thickness due to firn compaction and accumulation is close to zero in the entire study area (Fig. A4).
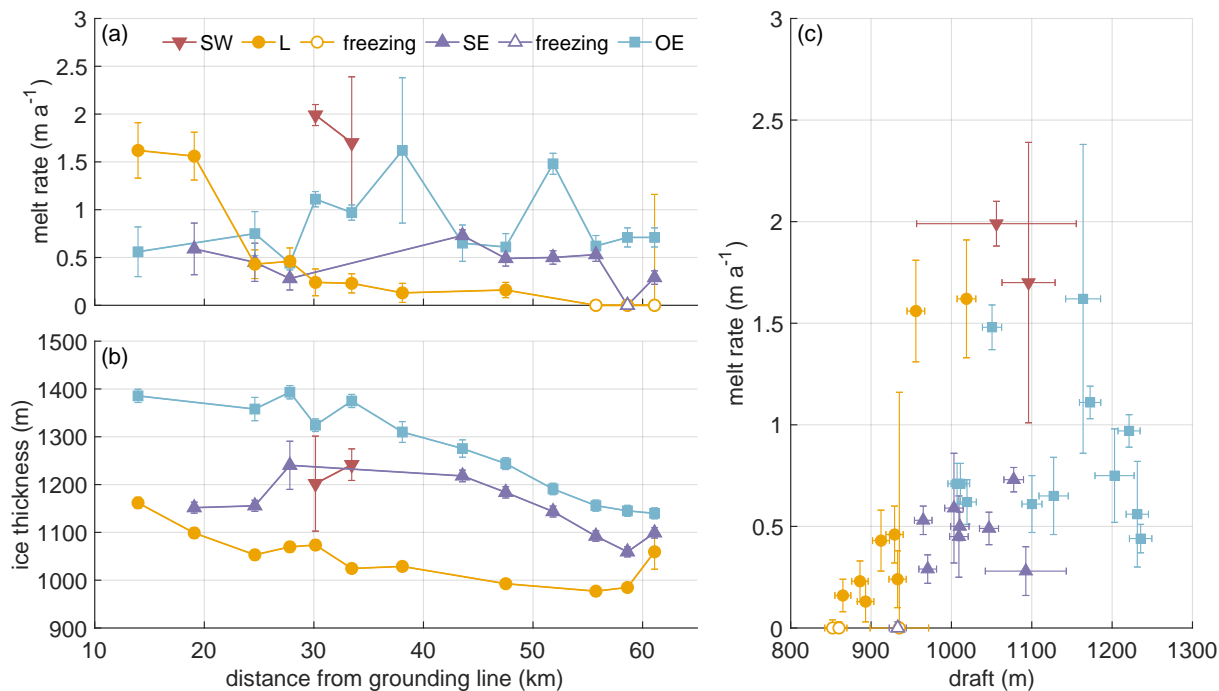
Figure 2. Spatial distribution of pRES-derived (a) basal melt rates (positive a_b represents melting) and (b) ice thickness at the locations SW (red), L (yellow), SE (purple) and OE (blue) around the channel as a function of distance from the grounding line. (c) Melt rate as a function of ice draft obtained from pRES-derived ice thickness and h_{TDX}.

However, the measurements only show a snapshot, as the variability on longer time scales is unknown. Based on the interpolated melt rates, ΔH_ε and ΔH_s along the channel (solid lines in Fig. 3a and A4), we computed the advected ice thickness under present day climate conditions H_{PDadv} (solid lines in Fig. 3b). The comparison of H_{PDadv} with the measured ice thickness

250   (dashed lines) shows large differences of up to $185\,\mathrm{m}$ above the channel. While the observed ice thickness decreases rapidly above the channel, H_{PDadv} remains almost constant. In contrast, no significant differences between the observed ice thickness and H_{PDadv} can be identified outside the channel. If the present day melt rates were representative of the long-term mean, the channel would close within 250 years, as the difference in H_{PDadv} above and outside the channel reaches zero. However, since the channel still exists beyond the northern end of our study area, it can be concluded that the melt rates in the channel must

255   have been higher in the past. How large the melt rates must have been on average can be deduced from the reconstruction of the existing ice thickness. The resulting synthetic average melt rate in the channel is about twice as high as the observed melt rates, reaching $3.5\,\mathrm{m\,a^{-1}}$ in the upstream area (yellow dashed line in Fig. 3a). Assuming a steady state ice thickness upstream of the

study area (supported by low elevation change found in (Helm et al., 2014)) and constant vertical strain and accumulation in the past, this indicates that melt rates in the last 250 years have been significantly higher than observed now.

In addition to the observations we have presented in this section, we show the pRES-derived vertical displacement profiles in section 3.2.2 together with simulations.
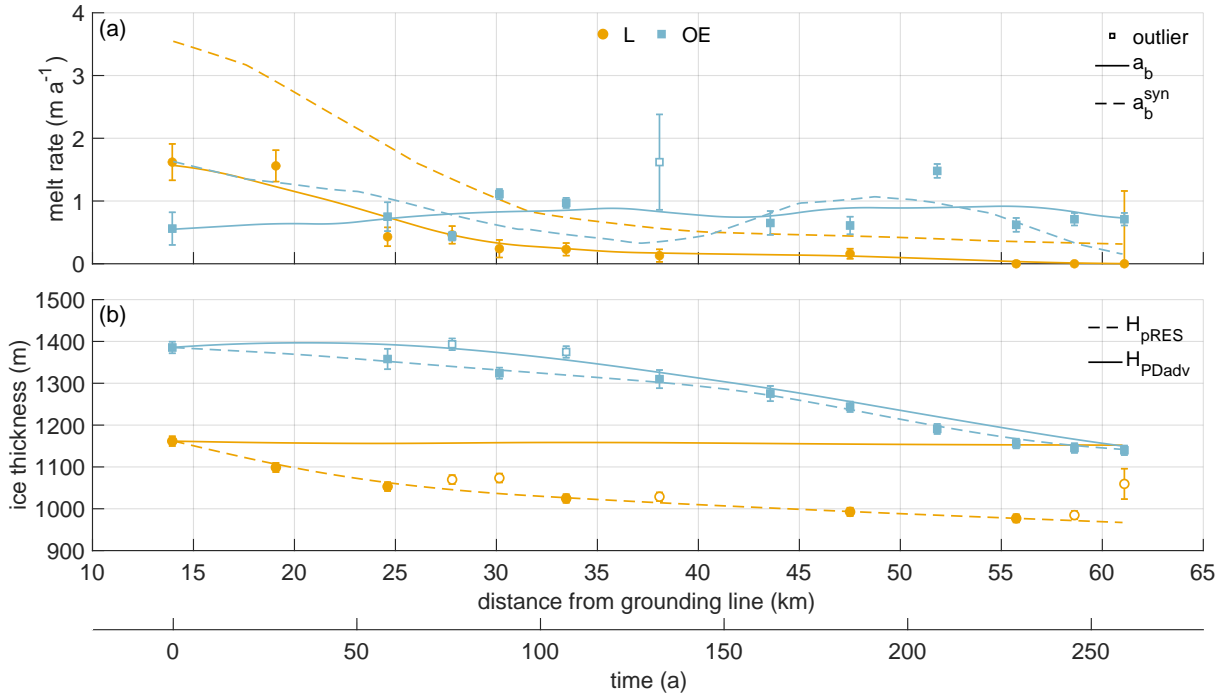
Figure 3. (a) Melt rates at locations L (yellow) and OE (blue) are shown by dots (L) and squares (OE). The interpolated melt rates (a_b) are shown by solid lines and synthetic melt rates (a_b^{syn}) that are necessary to reproduce H_{pRES} at L and OE are shown by dashed lines. (b) Ice thickness at locations L (yellow) and OE (blue) are shown by dots (L) and squares (OE). The interpolated ice thicknesses (H_{pRES}) are shown by dashed lines and the advected ice thicknesses under present day climate conditions (H_{PDadv}) from the observed melt rates at L and OE are shown by solid lines. The two x-axes show the distance from the grounding line in kilometers and the duration of ice flow in years from the measurement location furthest upstream. Unconsidered observations were marked as outliers. Error bars mark the uncertainties of the pRES-derived values.

2.3.2 Time series of basal melting

The ApRES time series outside the melt channel reveals an average melt rate of $0.23\,\mathrm{m\,a^{-1}}$ (Fig. 4a). A look at the monthly mean melt rates shows increased melt during the summer months (January, February and November, December) in comparison with the winter season. In these months the melt rates show values from more than $0.3\,\mathrm{m\,a^{-1}}$ up to $0.62\,\mathrm{m\,a^{-1}}$. The spec-

tral analysis of the unfiltered cumulative melt time series shows all main diurnal and semi-diurnal constituents, which is in accordance with the frequencies observed from the GPS station (Fig. A5).

The presence of the tidal induced signal prevents a robust analysis of the basal melt rate as a high resolution time series. Nevertheless, to investigate the occurrence of non-tidal melt anomalies, we analyzed the time series of $\Delta H(t)$ after it was 270 de-tided. The resulting de-tided thinning rate shows several melt anomalies distributed over the entire measurement period (Fig. 4b). These events lasted from a several hours to a few days and melted up to $1.5\,\text{cm}$ of ice. In comparison, the annual or seasonal signals have little impact on the thinning rate.
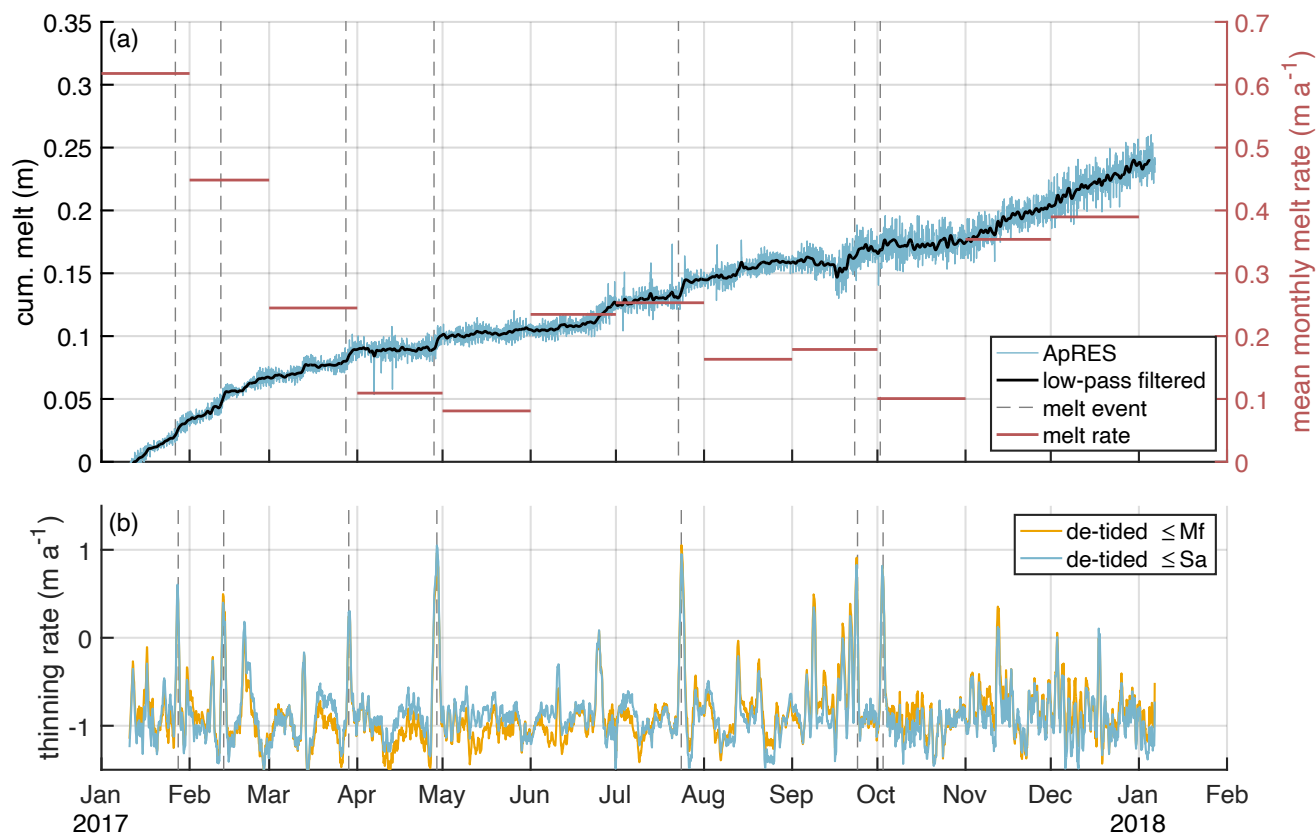
Figure 4. Time series of basal melting at ApRES location outside the channel. (a) Cumulative melt (blue line, left y-axis) over measurement period from 10 January 2017 to 6 January 2018 with low-pass filtered time series (black line). In September 2017, a malfunction of the ApRES caused a change of the attenuation which resulted in a noisier time series. Monthly mean melt rates are shown by red lines on the right y-axis. Due to the inaccuracy in the determination of the strain, the cumulative melt is still containing a contribution from strain. (b) Thinning rate after subtracting of the tidal signal up to the fortnightly constituent (yellow line) and up to the solar annual constituent (blue line). The dashed gray lines in (a) and (b) mark stronger melt events.

The unfiltered time series of the cumulative melt indicates a tidal signal with amplitudes of $\sim 1\,\mathrm{cm}$ within $12\,\mathrm{h}$ around the low-pass filtered cumulative melt. However, we found evidence that this tidal signal is due to the inaccuracy in the determination of the strain and not a true tidal melt amplitude: We found a clear accordance of the strain in the upper ice column with the tidal signal as recorded by GPS measurements, however, we are lacking tidal vertical strain in the lower column of the ice due to the noise. As the tidal variation of $\Delta H/\Delta t$ is by far lower than the observed $\Delta H_\varepsilon/\Delta t$, either deformation in the upper and lower parts compensates each other, or basal melt/freeze takes this role. We can exclude freezing, as we do not find jumps in the amplitude of the basal return in the ApRES signal (Vaňková et al., 2021) over tidal time scales. Consequently, we infer that strain in the lower half compensates that in the upper part and there is only a small variation of basal melt on tidal time scales.

As our location is close to two hinge zones, upstream and west of the melt channel, only a full three-dimensional model could shed light on the vertical strain in the lower part of the ice column. This is numerically costly for the required non-linear strain theory and beyond the scope of the project. With melt channels being located (or initiated) in the hinge zone, any kind of ApRES time series performed at thick ice columns might be affected by the unclear strain-depth profile in the lower part of the ice column. This may be overcome by a radar device with higher transmission power, that allows the detection of vertical displacement of layers down to the base. The observed tidal dependency of the vertical strain is consistent with the finding from other ApRES locations at the Filchner-Ronne Ice Shelf by Vaňková et al. (2020). They found the strongest dependency, even of the basal melt rate at some stations, on the semidiurnal (M_2) constituent. Besides depth-independent tidal vertical strain, Vaňková et al. (2020) found tidal deformation from elastic bending at ApRES stations located near grounded ice.

For an ice shelf such as the Filchner we expect the principal drivers of basal melting to be the water speed and its temperature above the in situ freezing point (e.g. Holland and Jenkins, 1999). For much of the ice shelf the water speed is dominated by tidal activity (Vaňková et al., 2020), but near the grounding line of SFG we expect the tidal currents to be low, consistent with the evidence from the ApRES thinning rate time series. It is likely that the anomalously high melting events seen in the record result from the passage of eddies, with their associated water speed and temperature anomalies.

3   Viscoelastic modeling

To obtain a more profound understanding of the evolution of the channel, we conduct transient simulations and analyze the change in geometry of 2D cross-sections (x, z direction) over time, as well as the simulated strain-field. The simulations are forced with the basal melt rates (both interpolated and synthetic) obtained in this study (Fig. 3). We transform distance (y-direction) to time in along flow direction of the ice shelf (Fig. 1) using present day velocities. This enables us to study under which conditions the channel is stable or vanishes.

Ideally, we would have observations of ice geometry and basal melt rates from the grounding line onward, but our first cross-section with observations is located $14\,\mathrm{km}$ downstream of the grounding line (Fig. 1). The initial elastic response of the grounded ice becoming afloat has faded away. Further elastic contributions to the deformation originate from in-situ melt at the base and accumulation at the surface. To best fit the stress-state at the first cross-section, we conduct a spin-up.

3.1 Model

The model comprises non-linear strain theory, as there is no justification to expect a priori the simplified, linearized strain description for simulation times longer than $200\,\mathrm{a}$ (e.g. Haupt, 2000). We treat the ice as a viscoelastic fluid and solve the system of equations for displacements using the commercial finite element software COMSOL (Appendix Sec. B1; Fig. B1 Christmann et al., 2019). The constitutive relation corresponds to a Maxwell material with an elastic response on short time scales and viscous response on long time scales. For homogeneous, isotropic ice, two elastic material parameters exist (Young's modulus E and Poisson's ratio ν). We conduct all viscoelastic simulations with commonly used values for ice of $E = 1\,\mathrm{GPa}$ and $\nu = 0.325$ (Christmann et al., 2019). Another material parameter of the viscoelastic Maxwell material is the viscosity. It controls the viscous flow of ice. We use a constant viscosity of $\eta = 5 \times 10^{15}\,\mathrm{Pa\,s}$ and discuss the influence of this material parameter later on. This constant viscosity is at the upper limit of the viscosity distribution derived by an inversion for the rheological rate factor in the floating part of the Filchner-Ronne Ice Shelf (Appendix Sec. B2 and Fig. B2). This inversion has been conducted using the Ice Sheet and Sea-Level System Model (ISSM) (Larour et al., 2012) in higher-order Blatter-Pattyn approximation (Blatter, 1995; Pattyn, 2003), using BedMachine geometry (Morlighem, 2020; Morlighem et al., 2020), the velocity field of Mouginot et al. (2019b, a), and a temperature field presented in Eisen et al. (2020), based on the geothermal heat flux of Martos et al. (2017). For the assumed material parameters, we obtain a characteristic Maxwell time of $\tau = 153\,\mathrm{d}$ by $\tau = (2 + 2\nu)\eta/E$ (Haupt, 2000).

The model geometry represents a cross-section through the melt channel (Fig. 5) with the x-direction being across channel and resembling the seismic IV profile (Fig. 1) for $t = 0\,\mathrm{a}$. By assuming plane strain, the shape and the loading do not vary in the along-flow direction (width is sufficiently large). The stress state is independent of the third dimension, the displacement u_y in flow direction is zero and hence all strain components in the direction of the width vanish

$$\varepsilon_{yy} = \varepsilon_{xy} = \varepsilon_{yz} = 0. \tag{10}$$

The computational domain is discretized by an unstructured mesh using prisms with a triangular basis involving a refined resolution near the channel. We use the direct MUMPS solver and backward differentiation formula with automatic time step control and quadratic Lagrange polynomials as shape functions for the displacements. The viscous strain is an additional internal variable in the Maxwell model and we use shape functions of linear Lagrange type. In some cases, the geometry evolution leads to degraded mesh elements, which requires automated remeshing from time to time.

In this study, the ice density is $910\,\mathrm{kg\,m^{-3}}$ and the seawater density is $1028\,\mathrm{kg\,m^{-3}}$. At the upper and lower boundaries, we apply stress boundary conditions: for the ice-ocean interface, a traction boundary condition specifies the water pressure by a Robin-type condition. The ice-atmosphere interface is traction-free. Laterally, we apply displacement boundary conditions. As we take a plane strain approach, we can neglect deformation in the along-flow direction. To obtain realistic lateral boundary conditions, we transform observed vertical strain and hence, vertical displacements, at the location OE in horizontal displacements. First, we assume incompressibility

$$\varepsilon_{zz}^{\mathrm{obs}} = -(\varepsilon_{xx}^{\mathrm{obs}} + \varepsilon_{yy}^{\mathrm{obs}}) \tag{11}$$

and compute the sum of the horizontal strain. We integrate this strain to get a horizontal displacement. Therefore, we assume a homogeneous material, no additional forces in horizontal direction and a constant ice thickness. The last assumption is not valid inside the channel. However with a channel of $300\,\mathrm{m}$ maximum height over $1\,\mathrm{km}$ width, the deviation from outside to inside the channel is small for a computational domain of around $10\,\mathrm{km}$ width and an ice thickness around $1300\,\mathrm{m}$. With these assumptions we get a constant strain and integrate this strain to get a horizontal displacement. As we additionally assume plane strain, we can only apply this displacement to the lateral boundary in the across-flow direction. To model the compression and extension of the ice flow through the embayment, we apply the horizontal displacement to each lateral side so that u_x becomes

$$u_x = \frac{1}{2} \int_0^W \left(\varepsilon_{xx}^{\mathrm{obs}} + \varepsilon_{yy}^{\mathrm{obs}} \right) dx = \frac{\left(\varepsilon_{xx}^{\mathrm{obs}} + \varepsilon_{yy}^{\mathrm{obs}} \right) W}{2}, \tag{12}$$

with W the width of the simulated cross-section (Fig. 5). We assume that the horizontal displacements are depth-independent at lateral boundaries, resulting in a compression or elongation perpendicular to the channel (Fig. B3a).

The climate forcing consists of SMB and basal melt rate. Technically, both are applied by changing the geometry of the reference configuration with the respective cumulative quantities (Fig. B3b,c). For the SMB, we used multi-year mean RACMO2.3 data (van Wessem et al., 2014) ranging from 0.15 to $0.17\,\mathrm{m\,a^{-1}}$ for a density of $910\,\mathrm{kg\,m^{-3}}$, that we slightly modified to account for the surface depression over the channel: accumulation measurements at the pRES locations indicated higher accumulation in the channel than outside by a factor of roughly 1.5. Thus, we used 50% higher accumulation rates above the basal channel and a smooth cosine-shaped transition in the x-direction. A crucial forcing is of course the basal melt rate. Here we conduct individual experiments that are based on our observed melt rates and their variations. As this data is spatially sparse, we need to interpolate those values in the across-channel (x) direction. We assume a smooth cosine-shaped transition between the observed basal melt rates outside east (OE) and inside the channel (L). For melt rates outside west, we do not have any observations and assume them to be time-independent. With 10% lower melt rates than for OE during the spin-up and a smooth cosine-shaped transition between outside west and lowest, we get a good agreement of the ice base geometry for outside west with seismic IV and V. For the first $20\,\mathrm{a}$ after the spin-up, the melt rate outside east is higher than outside west. While afterwards, the melt rates in the western part are higher than in the eastern part outside the channel.

As we conduct Lagrangian experiments, we computed the time between the observed measurements through their distance divided by flow velocity. We define $t_0 = 0\,\mathrm{a}$ at the pRES measurements furthest upstream (Fig. 1) that is also the location of the seismic observation IV by Hofstede et al. (2021a, b). To evaluate our simulations, we compare the simulated surface topography and ice thickness, as well as $u_z(z)$ with the observed one for the considered time interval of $250\,\mathrm{a}$.

We performed a spin-up to avoid model shocks, introduced by the transient behavior of a Maxwell material, that could be falsely interpreted as the response to geometry changes, for instance, caused by basal melt rates. The main goal here is to have the geometry after spin-up fit reasonably to the geometry measured at the seismic IV line (see Fig. 1) that we denote as time t_0. The spin-up covers 75 years, which corresponds to the time from the grounding line to that profile under present day flow speeds. To this end, we take a constant melt rate equal to the melt rate at t_0 and adjust the geometry at the grounding line to match the geometry at t_0 of the seismic IV profile reasonably well. After the spin-up, the width $W(t_0)$ of the simulated
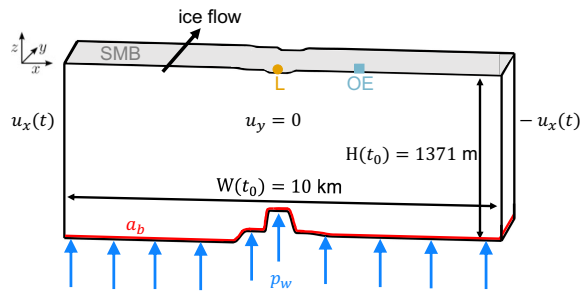
Figure 5. The cross-section of the model geometry at the end of the spin-up (t_0) of the first experiment shows its corresponding width and ice thickness outside east. The boundary conditions of the viscoelastic model are the water pressure p_w acting perpendicular to the ice base, the displacement in the flow direction u_y, which is zero due to plane strain assumptions, and the time-dependent displacement $u_x(t)$ acting in the flow direction derived by pRES observations. The locations of the pRES station at the lowest point (L) of the channel and outside east (OE) are shown at their position on the surface in addition to the SMB (mass increase) and the melt rate a_b (mass decrease) at the base of the geometry.

geometry is $10\,\mathrm{km}$. With this procedure the initial elastic deformation at the beginning of the transient simulation vanished and the viscoelastic geometry evolution of the melt channel can be evaluated for different melt scenarios and SMB forcings.

375 Short-term forces like the time-varying climate forcing as well as the lateral extension or compression demand the usage of a viscoelastic instead of a viscous model to simulate the temporal evolution of the basal channel shown later on. First, we conduct a series of simulations with different material parameters and identify the best match of observed and simulated ice thickness above (L) and outside east (OE) of the channel. At these two positions most of the pRES measurements were done and the distribution of the melt rates gives an adequate basis to force the model. Due to the sparsity of observations at the western side, we apply a forcing in the model based only on melt rates at L and OE.

380 In the first experiment, we use an interpolation of the observed melt rates as forcing and compare the results with H_{PDadv} (solid lines in Fig. 3). The second experiment aims to derive the best match between simulated and observed geometry. For this experiment, we use synthetic melt rates (dashed lines in Fig. 3a).

3.2 Results and discussion of simulations

3.2.1 First experiment: pRES-derived melt rate

385 The spin-up for this experiment starts with a manually adjusted geometry (including the channel at the base) at $t = -75\,\mathrm{a}$ to fit seismic IV profile at t_0. We applied a constant melt rate of $1.5\,\mathrm{m\,a^{-1}}$ at L and $0.5\,\mathrm{m\,a^{-1}}$ at OE. This forcing enlarges the melt channel during the spin-up as the ice thickness OE increases due to the prescribed displacement representing compression caused by the lateral boundaries moving towards the center of the channel. The general shape of the base matches the seismic profile IV reasonably well (Fig. 1 and Fig. B4). After the spin-up, we force the base with a_b (solid line in Fig. 3a).
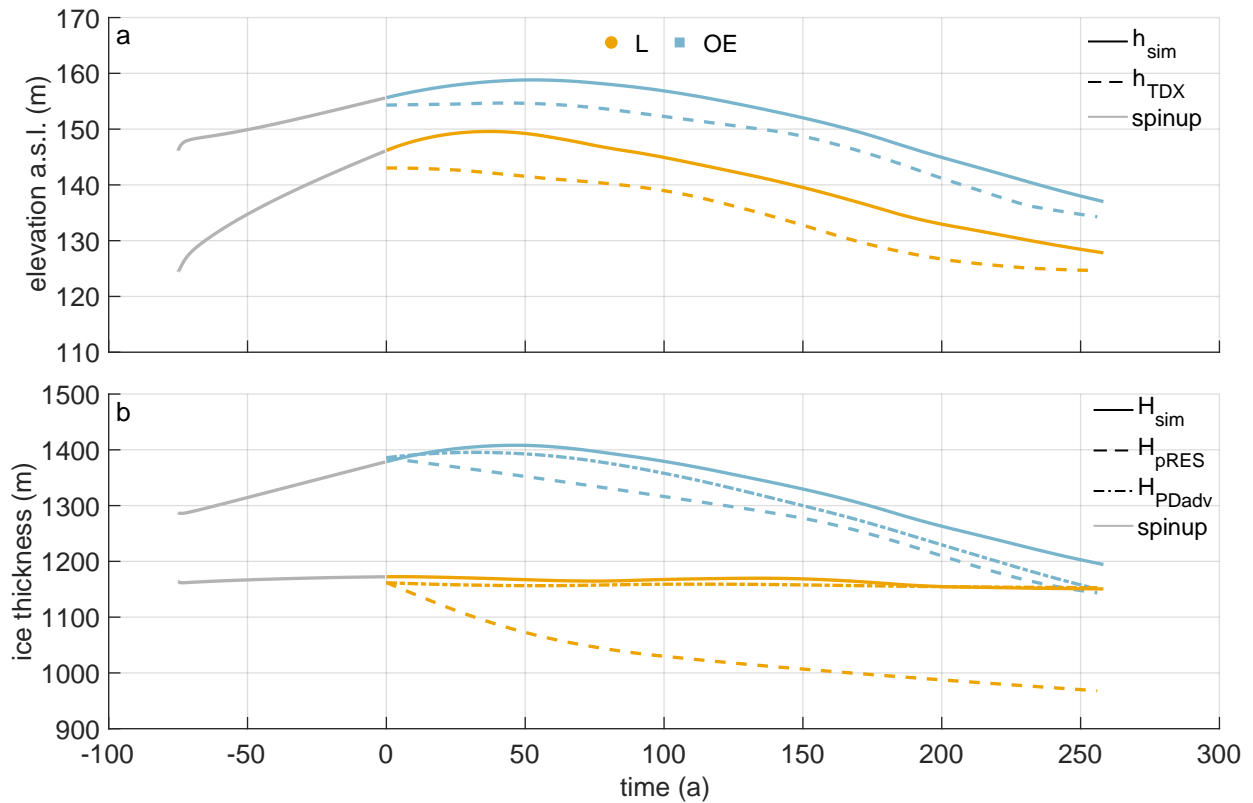
Figure 6. First experiment: Simulated surface elevation (a) and ice thickness (b) using the pRES-derived melt rate. Colors denote quantities above the channel (yellow) and outside the channel (blue). (a) Simulated surface elevation h_{sim} (solid lines) and observed h_{TDX} (dashed lines). (b) Simulated ice thickness H_{sim} (solid lines), under present day climate conditions advected H_{PDadv} (dashed-dotted lines) and observed H_{pRES} (dashed lines). Gray lines represent the spin-up.

390   The results of this experiment are displayed in Fig. 6. For both locations, L and OE, the simulated and observed geometry differ significantly. The simulated ice thickness above the channel declines by $21\,\text{m}$ in $250\,\text{a}$, while the observed thickness is $191\,\text{m}$ thinner. Outside the channel, the simulated trend shows thinning. This thinning begins after $50\,\text{a}$, whereas we find continuous thinning in the observations. This delayed onset of thinning is also represented in the simulated surface topography. Most notable is the match between simulated H_{sim} and advected H_{PDadv} ice thickness under present day climate conditions

395   at the center of the channel (L). At the same time, the mismatch to H_{pRES} confirms that present day melt rates would not lead to the observed channel evolution over $250\,\text{a}$.

3.2.2 Second experiment: Synthetic melt rate

The spin-up for the second experiment starts with a different geometry than the first experiment as the basal melt rate is different. However, it has also been manually adjusted at $t = -75\,\mathrm{a}$ to fit seismic IV profile at t_0. In the second simulation experiment, we force the base with the synthetic melt rate (Fig. 3a) that is larger inside the channel than the observed melt rate. Again, the melt rate has been kept constant over the spin-up with $a_b^{\mathrm{syn}}(t_0)$. The synthetic melt rate leads to a cumulative melt after $250\,\mathrm{a}$ of $290\,\mathrm{m}$ (Fig. B3a) with $184\,\mathrm{m}$ more ice melted at L than in the first experiment and hence, the initial geometry has to be different to the first experiment, hence we conduct an own spin-up simulation for the second experiment.

The modeled geometry of this experiment is presented in Fig. 7. The simulated ice thickness at L is in very good agreement with H_{pRES}. There is some mismatch at OE, but the simulated trend of thinning is synchronous to the observations. After $250\,\mathrm{a}$ the deviation from the observed ice thickness at OE reaches $+53\,\mathrm{m}$. The simulated base for the second experiment shows a persistent basal channel (Fig. B5). The mismatch of the surface elevation at L and OE reverses over time: while the simulated surface topography at OE is first too low, it is too high in the second half of the transient simulation (Fig. 7). However, the trend of the observed h_{TDX} and simulated h_{sim} elevation behave similarly. While ice thickness is in good agreement, surface elevation above the channel is overestimated by $4\,\mathrm{m}$ at the end of the spin-up. After $57\,\mathrm{a}$, it turns from an over- to underestimation that results in an $8\,\mathrm{m}$ lower h_{sim} than the observed h_{TDX} after $250\,\mathrm{a}$. To understand if the ice is in hydrostatic equilibrium, we compute the freeboard at the position L for an ice density of $910\,\mathrm{kg\,m^{-3}}$. The surface elevation is $133\,\mathrm{m}$ at t_0 and decreases to $112\,\mathrm{m}$ after $250\,\mathrm{a}$. Although h_{TDX} is larger than this, the ice is approaching flotation in the downstream direction. One could take another approach and estimate the mean density under the assumption of buoyancy equilibrium: at t_0 this corresponds to $901\,\mathrm{kg\,m^{-3}}$ and after $250\,\mathrm{a}$ to $896\,\mathrm{kg\,m^{-3}}$. As more ice is melted from below and with higher snow accumulation at L, the density decreases, which is to be expected.

After $250\,\mathrm{a}$, the simulated freeboard at L is $1\,\mathrm{m}$ higher than the surface elevation of $138\,\mathrm{m}$ inferred by buoyancy equilibrium using an ice density of $910\,\mathrm{kg\,m^{-3}}$ and at OE the discrepancy is $3\,\mathrm{m}$. Overall, we see convergence to equilibrium state at OE and the simulated surface elevation at L. At the end of the simulation, only h_{TDX} above the channel does not reach buoyancy equilibrium, which leads to the justifiable assumption that the mean ice density at L is lower than OE.

At the position of the furthest upstream pRES observations we know from interferometry shown in Hofstede et al. (2021a) that the location is still in the hinge zone. The assumption of buoyant equilibrium is therefore likely to be flawed. At the end of the simulation, the geometry should be close to buoyancy equilibrium despite melting and a 50% higher SMB at L than OE. Hence, simulations carried out using a higher SMB within the channel would result in better agreement with the observed values of h_{TDX}.

Next, we consider the variation of the vertical displacement with depth. The results are presented in Fig. 8. For this purpose, we calculated the cumulative vertical displacement in one year. For comparability, the vertical displacements due to accumulation and snow compaction were removed from the observed distributions. Most notably, we move from a vertically extensive regime to a compressive regime with increasing distance from the grounding line. Given the complexity of the problem, the
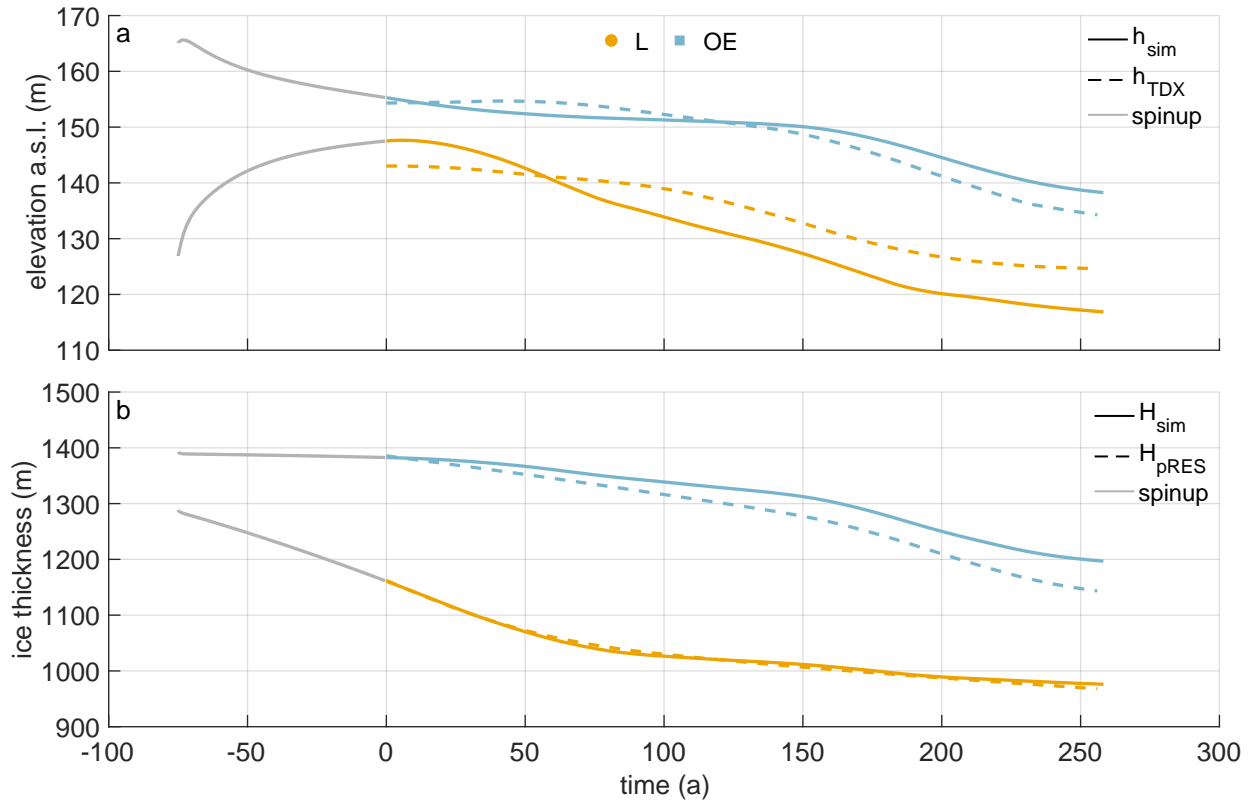
Figure 7. Second experiment: simulated surface elevation (a) and ice thickness (b) using the synthetic melt rate. Colors denote quantities above the channel (yellow) and outside the channel (blue). (a) Simulated surface elevation h_{sim} (solid lines) and observed h_{TDX} (dashed lines). (b) Simulated ice thickness H_{sim} (solid lines) and observed H_{pRES} (dashed lines). Gray lines represent the spin-up.

simulations show a reasonable agreement with the observations. The best match is reached at OE, which is not that surprising. The generally good agreement of the simulated displacements outside the channel comes from tuning u_x at the lateral boundary to match u_z from the pRES measurements at OE. A schematic illustration of first principal strains and their directions shows a closure of the channel for lateral compression and simultaneously a thickening of the ice shelf that is larger inside the channel than outside (Fig. B6). For lateral extension, we conversely get a thinning of the ice shelf that is smaller inside the channel than outside. Both simulated and observed vertical displacement distributions show that the strain decreases from L to OE (Fig. 8). The only exception here is $t = 57\,\mathrm{a}$, where the vertical strain at SE is larger than the one at L, in the observations. While at $0\,\mathrm{a}$ and $26\,\mathrm{a}$ the deviation of the simulated displacements between L and OE is small, it increases afterwards. From $105\,\mathrm{a}$, the simulated vertical displacements agree very well with those of the pRES-measurements, where a displacement distribution was derivable at L and OE. The same comparison for the first experiment (Fig. B7) shows similar results, with significantly less
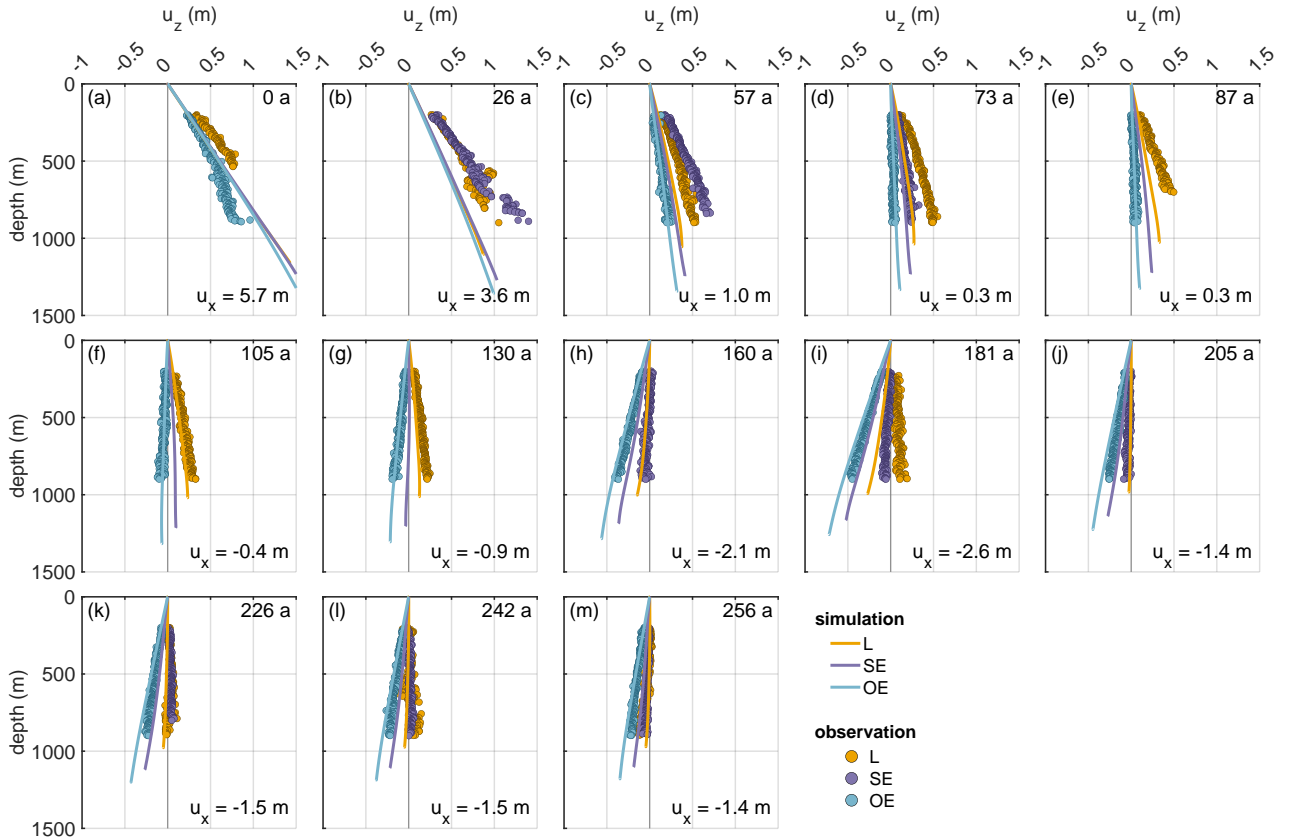
Figure 8. Second experiment: comparison of displacements (u_z) derived from observations (dots) and the simulations (lines). The different panels show the displacement for $\Delta t = 1\,\mathrm{a}$ allocated to the simulation time (upper right corner). The numbers in the lower right corners give horizontal displacement u_x derived from ε_{zz} of the pRES measurements outside the channel (OE) with positive values representing compression and negative values extension.

pronounced differences between L and OE. Hence, the mismatch to the observed vertical displacements for this experiment using the measured melt rates is higher than for the second experiment with the synthetic melt rates.

As the last point of this second experiment, we consider the influence of the viscosity on the evolution of the melt channel (Fig. B8). To reach the ice thickness of seismic IV, the simulation applying the smallest viscosity needs a higher initial channel at the beginning of the spin-up (Appendix Sec. B3). The channel thickness of the pRES-measurement is modeled best using a viscosity of $5 \times 10^{15}\,\mathrm{Pa\,s}$. A two times higher viscosity leads to a geometry where the ice is $42\,\mathrm{m}$ thinner in the center of the channel after $250\,\mathrm{a}$, while a five times lower viscosity results in $116\,\mathrm{m}$ thicker ice above the channel due to more viscous flow into the channel. The simulated ice thickness OE is similar for all three different viscosities. The distributions of vertical displacement with depth illustrate that the difference between L and OE is larger for smaller viscosity values (Fig. B9). Often

445

450   the viscosity of $5 \times 10^{15}\,\mathrm{Pa\,s}$ fits quite well to obtain the observations by the simulation but for some a slightly (Fig. B9a) or a considerably lower viscosity (Fig. B9c) would be needed.

    We also conducted simulations to test with extreme high melt rates along the steep slopes at the flanks, which did not lead to a reasonable evolution of geometry of the channel and they are therefore not presented here.

4   Discussion

455   First we aim to compare our findings with other measurements inside a melt channel, which are unfortunately still very sparse and we want to emphasize here, that there is a strong need for more of this type of observation in future. We find that melt rates inside the channel are in general rather modest, $< 2\,\mathrm{m\,a^{-1}}$. Values retrieved at a channel $1.7\,\mathrm{km}$ from the grounding line at the inflow of the Mercer and Whillans ice streams into the Ross Ice Shelf were $22.2\,\mathrm{m\,a^{-1}}$ (Marsh et al., 2016). These values dropped to below $4\,\mathrm{m\,a^{-1}}$ over a distance of $10\,\mathrm{km}$ and reached $2.5\,\mathrm{m\,a^{-1}}$ after $40\,\mathrm{km}$. We also find that the melt rates decrease

460   by a factor of five in the center of the channel over a distance of $11\,\mathrm{km}$, however, this takes place between 14 and $25\,\mathrm{km}$ downstream the grounding line. At the Ross Ice Shelf, the ratio between the melt rates inside the channel and $1\,\mathrm{km}$ outside it is about 27, whereas we find only a factor of 3, with the distance between L and OE being $1.8\,\mathrm{km}$.

    Zeising et al. (2022b) presented pRES-derived basal melt rates downstream of our study area. Roughly $40\,\mathrm{km}$ downstream

465   the northernmost cross-section ($\sim 200\,\mathrm{a}$ of ice flow), these measurements show that the channel still exists, but with a small height of $\sim 16\,\mathrm{m}$. Inside the channel, Zeising et al. (2022b) determined a melt rate $\sim 0.20\,\mathrm{m\,a^{-1}}$ lower than outside. The larger melt rates outside the channel compared to inside is in agreement with the finding of our study. In general, the channel height declines, so the channel fades out. The channel diminishes because melt rates inside the channel fall below those outside the channel. The trend in vertical strain has only a minor contribution to this evolution. We thus do not find any evidence that such

470   channels are a cause for instabilities of ice shelves as suggested by Dow et al. (2018).

    One of the main findings of our study is that the present geometry can only be formed with considerable higher melt rates in the past (see Fig. 3). This finding is based on the assumption that the strain-rates were in the past similar to present day and that melt on both flanks of the channel are similar. This is justified, as significant changes in strain would require a change in the system that would cause other characteristics to change, like the main flow direction, for which we do not find any indication.

475   However, in our setting, we are in a compressive regime. A similar assumption may at other locations not be possible.

    The pRES melt rate observations covered only one year. As the ocean conditions within the sub-ice shelf cavity are known to respond to the ocean forcing from the ice front (e.g. Nicholls, 1997), we would expected them to be subject to significant interannual variability. Underlying any interannual variability, a long-term reduction in basal melt rates would be the expected response to a reduction in production of dense shelf waters north of the ice front, resulting from a reduction in sea ice formation

480   (Nicholls, 1997), resulting in turn from a reduction in the southerly winds that blow freshly produced sea ice to the north.

    A decrease in northward motion of sea ice has been observed in the satellite record (e.g. Holland and Kwok, 2012), but no observation of sea ice trends over $250\,\mathrm{a}$ is available to our knowledge. The modeling experiments by Naughten et al. (2021)

also find decreasing ice-shelf basal melt rates. This reduction is therefore consistent with higher basal melt rates in the past. However, our model results suggest that the mismatch between the past melt rates needed to explain the channel geometry and the present-day observed melt rates applies only to the channel, and not to the ambient ice. This could be explained by historically higher levels of subglacial outflow at the grounding line, or anomalously low levels during the observation period. Subglacial outflow contributes to the buoyant flow up the basal slope and therefore the shear-induced turbulence that raises warm water from deeper in the water column towards the ice base. Variations in the subglacial outflow could be caused by variations in subglacial storage, as Smith et al. (2009) found an active subglacial lake at the transition between Academy Glacier and SFG, and Humbert et al. (2018) also suggest the presence of a subglacial lake in the upstream area of SFG.

Hofstede et al. (2021a) showed that the subglacial channel appears $7\,\mathrm{km}$ upstream of the grounding line increasing its height to $280\,\mathrm{m}$ at the grounding line. The location of the channel corresponds with increased subglacial flux found by Humbert et al. (2018) using a simple routing scheme. Once this topographic feature reaches the ocean, it serves to focus the buoyant plume and enhance shear-driven vertical mixing, bringing heat and salt to the ice base leading to higher basal melt rates.

However, with increasing distance along the channel, the basal gradient, and therefore the speed of the buoyant flow, is reduced, which also reduces the entrainment of warm water from beneath. Coupled with the pressure-induced increase in the freezing point with decreasing depth, this leads to a gradual reduction of the melt rate in the channel. From Fig. 2a, the melt rate in the channel reduces below that of the ambient ice base by about $30\,\mathrm{km}$ distance from the grounding line, suggesting that the effect of focused meltwater outflow thereafter is to suppress the channel.

The cause of the strong melt anomalies identified in the ApRES measurements remains unclear as no direct ocean observation exists near SFG. However, the time scale of the events is consistent with the passage of warm cored eddies. Such features have been observed in the ocean cavity beneath the neighboring Ronne Ice Shelf (Nicholls, 2018).

The channel height is found to increase until $30\text{--}35\,\mathrm{km}$ downstream of the grounding line. Further downstream, the channel begins to close. Our modeling results show that less viscous ice ($1\times10^{15}\,\mathrm{Pa\,s}$) would tend to shut the channel faster than the rate we observe (Fig. B8). For the best match between observed and modeled geometry, we need viscosities around $5\times10^{15}\,\mathrm{Pa\,s}$ to prevent closure by deformation (Fig. 7). This viscosity value is also supported by an inversion of ice rheology to fit observed surface velocities in the melt channel region (Appendix Sec. B2). With a viscosity of $5\times10^{15}\,\mathrm{Pa\,s}$, we can use a viscoelastic model to simulate the channel evolution in both experiments to match the observations: (i) pRES-derived melt rates result in an ice thickness fitting the present day advected ice thickness H_{PDadv} (Fig. 6), and (ii) synthetic melt rates lead to the observed ice thickness H_{pRES} (Fig. 7). The channel vanishes for the pRES-derived melt rates as those are unable to maintain the channel geometry open against viscoelastic deformation (Fig. B4). Based on the higher synthetic melt rates, the simulated basal channel remains open and we get a similar basal shape to that found by the seismic measurements (Fig. B5). However, if we would want to match the observed basal geometry at seismic profile V more precisely, we would have to spatially vary the basal melt rate in the across-flow direction, enlarge the transition between L and OE, and thus extend the channel to the eastern side.

To evaluate the importance of using a viscoelastic and not a purely viscous material law, we compute the logarithmic Hencky strain (Appendix Sec. B4). With this strain measure, an additive decomposition of the strain into an elastic and viscous part is

possible. After the spin-up, the elastic strain components in the across-flow and thickness direction are on the order of 0.1% and one order of magnitude larger than the shear component (Fig. B10). Christmann et al. (2021) derived similar magnitudes in the viscoelastic simulation of $79°$ North Glacier considering linearized strains. The magnitude of elastic strain in the across-flow direction is caused by the lateral compression and varies slightly to higher values around the channel due to the geometry of the channel. However, the highest elastic strain values are reached outside the channel and decrease with time (Fig. B11). It is likely that the elastic deformation slightly increases especially inside the channel if the lateral compression changes into tension or vice versa. In the thickness direction, the elastic strain is decreasing towards the channel (Fig. B10b). This causes the difference in geometry change, due to different values of the viscosity, to be larger inside the channel rather than outside (Fig. B8). The simulated geometry change is mainly due to the elastic response to thinning by basal melt and ice accumulation. Any purely viscous simulation would overrate the deformation in the vertical direction as the elastic strain has the opposite sign as the viscous one (Fig. B12d-f). Higher melt rates were needed to compensate for this. Wearing et al. (2021) presents a full Stokes simulation of a comparable melt channel and indeed needs higher melt rates to keep the channel open. The relative amount of elastic strain shows values up to 8% of the total strain for high lateral compression or extension and is hence not negligible (Fig. B10). It is important to keep this result in mind for future inverse modeling of melt rates in melt channels.

We find a difference ($-4\,\mathrm{m}$ to $8\,\mathrm{m}$) between simulated and observed surface elevation at L (Fig. 7). The elevation difference is most likely caused by the constant density that we used for the simulations, as the ice thickness matches well. For the thinner ice above the channel, this could be achieved by an ice density decreasing from outside to inside and from upstream to downstream in the channel. However, one has to keep in mind that the accuracy of the surface elevation product is only $5\,\mathrm{m}$, so the differences in surface elevation may not be significant.

In general, we benefited highly from having measurements of vertical strain available. This opens new possibilities to identify weaknesses in the modeling, such as limited knowledge on lateral boundary conditions and rheological parameters, and gave us useful insight into the spatial variation of the vertical strain across such a topographic feature (Figs. 8 and B7). Although the pRES surveys only about half the ice thickness, the slope of $u_z(z)$ in the upper half is distinct for the positions L, SE and OE and greatly varies with distance from the grounding line, and is also influenced by the embayment of the ice shelf. Simulated u_z at L starts to match well with observations after about $100\,\mathrm{a}$, which could result from the first few cross-sections still being influenced by the hinge zone (Fig. 8). Tidal bending was not taken into account here, due to the 2D setting. This could in future be investigated, if repeated pRES measurements would be conducted up to the grounding line covering the entire hinge zone, in which case it would also be extremely advantageous to obtain basal melt rates at tidal time scales. In addition, in future melt rates should be obtained on both flanks of the melt channel, as well as having an coverage of the melt channel with airborne surveys to have detailed knowledge of the entire 3D geometry.

Our study demonstrates that viscoelastic simulations can be a useful but complex tool to analyze melt channel evolution. In an inverse approach, viscoelastic models could also give more insights into basal melt rates of channel systems of ice shelves in general, given that satellite-borne surface elevation is available in high resolution. However, the fact that large deformations require non-linear strain theory will make this a challenging endeavor. As changes in basal melt rates will inevitably lead to

surface elevation changes of channel systems, systematic monitoring of the surface topography from space can serve as an early warning system and trigger further in-situ observation similar to this study.

5 Conclusions

555 We find basal melt rates in a melt channel and its surroundings on Filchner Ice Shelf to be up to $2\,\mathrm{m\,a^{-1}}$. Basal melt rates inside the channel drop with distance down-flow, even turning into freezing $55\,\mathrm{km}$ downstream of the grounding line. Close to the grounding line, melt rates are larger inside the channel than outside, while further downstream this relationship reverses. Along flow, the channel height decreases from a maximum of $330\,\mathrm{m}$ to below $100\,\mathrm{m}$. The channel diminishes because the reduced melt rate is unable to maintain the channel geometry against viscoelastic deformation. Analysis of the predicted ice thickness
560 from advection of present-day thickness with present-day melt rates revealed large differences compared to the observed ice thickness above the channel, which indicates that melt rates have been about twice as large in the last $250\,\mathrm{a}$. The viscoelastic simulation confirms this statement and indicates that basal melt channels need high basal melt rates and relatively cold ice to persist. The deformation of the basal melt channel is mainly driven by the elastic response to the basal melt rate. The observed and simulated evolution of this melt channel demonstrates that melt channels of this kind (where melt rates inside the channel
565 are small and turn to freezing downstream) are not a destabilizing element of ice shelves. The ApRES time series showed brief melt anomalies distributed over the entire measurement period and slightly increased melt rates in summer.

Code availability. The mph file of the finite element software COMSOL Multiphysics (Version 5.6) of the viscoelastic finite deformation simulation used for this study is available via AWI's gitlab (https://gitlab.awi.de/jchristm/viscoelastic-finite-defos-meltchannel).

Data availability. Raw data and derived products of the single-repeated pRES measurements (https://doi.pangaea.de/10.1594/PANGAEA.941400,
570 Zeising et al., 2022a), raw data of the ApRES time series (https://doi.org/10.1594/PANGAEA.932413, Zeising et al., 2021b), surface accumulation data at pRES locations (https://doi.org/10.1594/PANGAEA.940252, Zeising et al., 2021c) and processed GPS measurements (https://doi.org/10.1594/PANGAEA.932441, Zeising et al., 2021a) are published at the World Data Center PANGAEA. The seismic data (https://doi.org/10.1594/PANGAEA.932278) are available at the World Data Center PANGAEA (Hofstede et al., 2021b). BedMachine Antarctica product can be accessed at http://nsidc.org/data/nsidc-0756200 (Morlighem, 2020) (last access: 12 April 2021). MEaSUREs
575 velocity product can be accessed at https://nsidc.org/data/nsidc-0754/versions/1 (Mouginot et al., 2019a) (last access: 13 April 2021).

Appendix A: Observations

A1 Basal reflections and the influence of off-nadir returns

The identification of the basal reflections in both measurements, the first and the repeat measurement, is important in order to determine the change in ice thickness and thus the basal melt rate. Due to a high contrast in relative permittivity, the ice—ocean interface is a particularly strong reflector. Accordingly, the reflection at the ice base in the echogram is characterized by a sharp increase in amplitude. After identifying the first basal reflection in both measurements, the vertical displacement can be determined by means of a cross-correlation of the basal segment, provided that the shape of the basal reflector has not changed significantly. However, this was not the case at five of the 44 stations in our study area. At these, the basal return had changed significantly and thus prevented an unequivocally match. We therefore excluded these stations from the melt rate analysis. At all other stations, the reflection had changed only slightly, so that the vertical displacement could be reliably determined. Figure A2 shows three examples (OE, SE and L) from a cross-section 48 km downstream of the grounding line. In all of these measurements, a strong increase in amplitude was found between 992 m (L) and 1244 m (OE), which represents the first onset of the basal reflections. While the shape of the basal return changed only slightly, there was a change in amplitude, which is lower in the repeat measurement, especially in Fig. A2e,f. One potential reason for this was different measurement settings that influenced the amplification of the signal, but imprecise alignment of the transmitting and receiving antennas can also be responsible for this.

However, at 7 of the 44 stations more than one strong and clear defined basal reflection was found, raising the question of which is the nadir and which is the off-nadir reflection. The reason for this is that a steep base, such as on the flanks of the channel, creates strong off-nadir reflections. Depending on the basal gradient, this off-nadir reflection may also arrive before the nadir reflection. As pRES data represent point measurements, they cannot be used to constrain the local shape of the ice base and thus distinguishing nadir from off-nadir returns is difficult. One possible indicator of the nadir reflection can be the reflection amplitude, since the antenna radiates most of its energy in the nadir direction. However, in certain basal geometries off-nadir reflections can still be stronger than the nadir reflection, even accounting for the antenna beam pattern. Figure A3 shows two examples of stations with off-nadir reflections. In the measurements at the pRES029 station (OE; Fig. A3a,b), the basal reflection with the largest amplitude appeared with a range 11 m greater than the first basal reflection. This could be an indication that the first basal reflection is an off-nadir return. The analysis of the vertical displacement of both basal reflections shows a deviation of 0.13 m. The second example from station pRES019 (SW; Fig. A3c-e) shows two basal reflections of approximately equal strength, separated by about 175 m. At this station, the deviation of the vertical displacement of both basal returns was only 0.01 m. Which of these reflections is the nadir and which is the off-nadir reflection cannot be reliably determined from the pRES measurement. Only by analyzing the basal geometry, e.g. by airborne radar or seismic profiles, can the reflection be assigned to its place of origin by determining the basal distances from the measurement location. However, since seismic profiles are only available in the vicinity of two cross-sections, this method cannot be used for all stations. Thus, we calculated the displacement of the second and strongest basal return of those 7 stations where more than one strong basal return occurred. The melt rates derived from the first and the second basal return are shown in Tab. A1. While at 3 sites the

difference in melt rate is below $0.1\,\mathrm{m\,a^{-1}}$, at others, the melt rate difference exceeds $1\,\mathrm{m\,a^{-1}}$. Since we cannot distinguish between nadir and off-nadir solely from our pRES measurements, we have averaged the two derived melt rates and take into account the difference in the error. However, at station pRES042 (L) we found basal freezing by analyzing the first basal return but derived a melt rate of $1.09\pm0.07\,\mathrm{m\,a^{-1}}$ from the second, stronger basal return. We designate this location as a basal freezing station and state the range of melt rate as an error.

A2 Additional table

Table A1. Melt rates determined from different basal returns.

pRES station	location	basal return #1		basal return #2		Average	
		range (m)	a_b $(\mathrm{m\,a^{-1}})$	range (m)	a_b $(\mathrm{m\,a^{-1}})$	range (m)	a_b $(\mathrm{m\,a^{-1}})$
pRES016	SW	1221.0±12.2	1.09±0.08	1262.3±12.6	2.32±0.07	1241.7±33.0	1.70±0.69
pRES019	SW	1114.6±11.2	1.97±0.09	1289.3±12.9	2.02±0.09	1202.0±99.4	1.99±0.11
pRES020	SE	1202.4±12.0	0.28±0.12	1278.3±12.8	0.27±0.12	1240.3±50.4	0.28±0.12
pRES025	OE	1347.2±13.5	0.89±0.10	1368.8±13.7	0.61±0.09	1358.0±24.4	0.75±0.23
pRES028	OE	1301.3±13.0	2.29±0.09	1318.6±13.2	0.95±0.09	1310.0±21.8	1.62±0.76
pRES029	OE	1269.9±12.7	0.60±0.13	1280.8±12.8	0.70±0.14	1275.4±18.2	0.65±0.19
pRES042	L	1033.6±10.3	freezing	1085.2±10.9	1.01±0.07	1059.4±36.4	freezing – 1.09±0.07

Table A2. Description of symbols

Symbol	Description	Unit
u_x	horizontal displacement in across flow	m
u_y	horizontal displacement in along flow	m
u_z	vertical displacement	m
$\varepsilon_{xx}^{\mathrm{obs}}$	horizontal strain in across flow	
$\varepsilon_{yy}^{\mathrm{obs}}$	horizontal strain in along flow	
$\varepsilon_{zz}^{\mathrm{obs}}$	vertical strain	
$\overline{h_b}$	averaged depth of the ice base	m
h_{pc}	depth of the pore closure relative to surface	m
h_{nl}	noise-level depth limit relative to surface	m
h_{sim}	simulated surface elevation	m
h_{TDX}	TanDEM-X surface elevation	m
H	ice thickness	m
H_{pRES}	pRES derived ice thickness	m
H_{sim}	simulated ice thickness	m
H_{PDadv}	advection of the ice thickness under present day climate conditions	m
t	time	a
t_0	$t = 0\,\mathrm{a}$, defined at the most upstream pRES measurement location	a
t_1	1st measurement of ApRES time series	
t_i	i-th measurement of ApRES time series	
Δt	time period between repeated measurements	a
ΔH	change in ice thickness	m
ΔH_i	change in ice thickness below the depth of the pore close	m
ΔH_s	change in ice thickness at the surface and in the firn	m
ΔH_f	change in ice thickness due to firn compaction	m
ΔH_ε	change in ice thickness due strain	m
ΔH_b	change in ice thickness due to basal melt	m
a_b	basal melt rate	$\mathrm{m\,a^{-1}}$
a_b^{syn}	synthetic basal melt rate	$\mathrm{m\,a^{-1}}$
W	width of the cross-section in simulations	m

A3   Additional figures
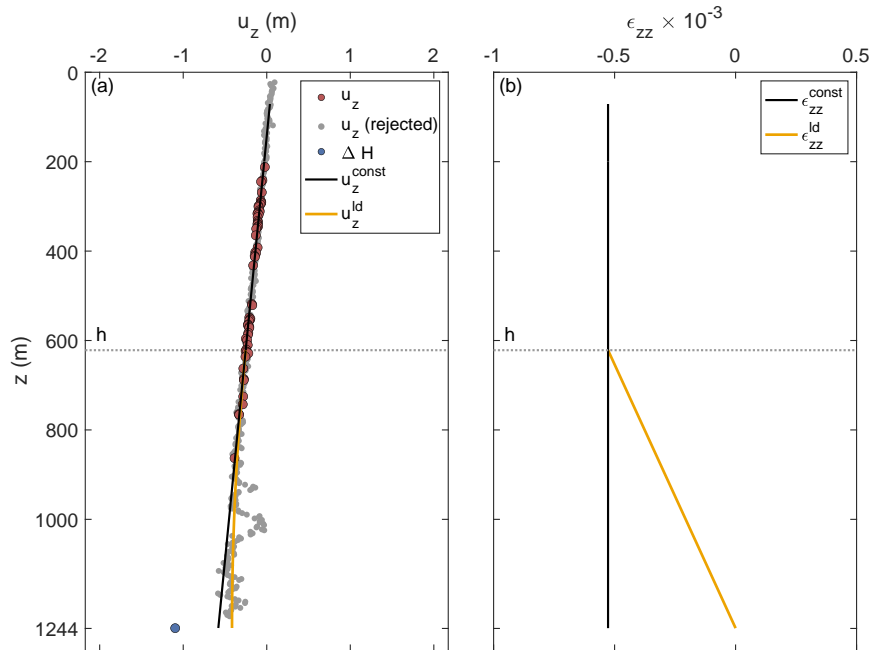
Figure A1. Strain analysis of a pRES measurement at location OE (pRES30; 48 km from grounding line). (a) Derived vertical displacements u_z for $\Delta t = 1\,\mathrm{a}$ of the ice base (ΔH; blue dot) and internal layers (red and gray dots). Displacements used for the linear regression u_z^{const} (black line) are colored in red and rejected displacements are shown in gray. The second model u_z^{ld} with a linear decreases (ld) from depth h (dotted line) to zero at the ice base is shown in orange. (b) Vertical strain for $\Delta t = 1\,\mathrm{a}$ of both models whose displacement is shown in (a).
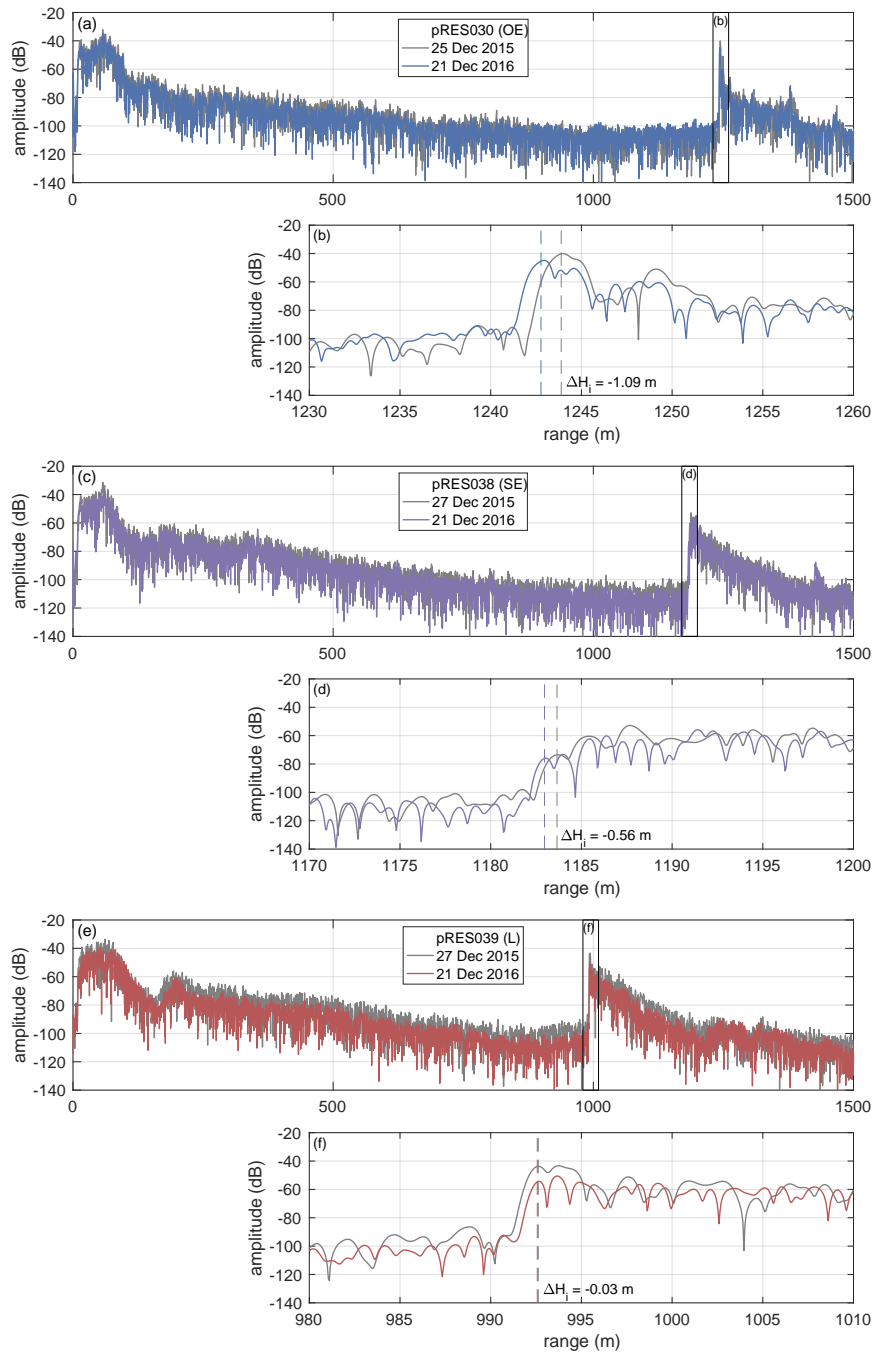
Figure A2. Amplitude profiles of first (gray line) and repeated pRES measurements at locations OE (a, b; blue), SE (c, d; purple) and L (e, f; red), all at the cross-section with a distance of 48 km from the grounding line. (b, d, f) Enlarged basal section, visualized by black boxes in (a), (c) and (e). Vertical dashed lines mark the ice thickness and ΔH_i the change in ice thickness between both visits.
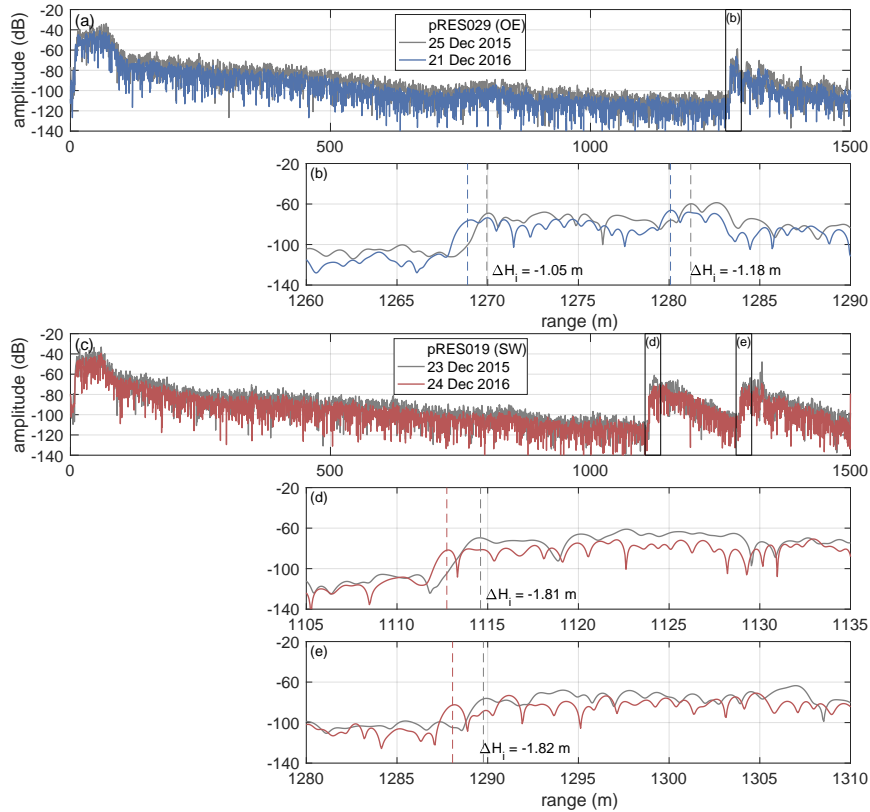
Figure A3. Amplitude profiles of two measurements indicating off-nadir basal reflections. (a, b) First (gray line) and repeated pRES measurement (blue) at location OE at the cross-section with a distance of 43 km from the grounding line. (b) Enlarged basal section, visualized by black boxes in (a). Vertical dashed lines mark the ice thickness and ΔH_i the change in ice thickness between both visits for the first and second strong increase in amplitude. (c–e) First (gray line) and repeated pRES measurement (red) at location SW at the cross-section with a distance of 28 km from the grounding line. (d, e) Enlarged basal sections, visualized by black boxes in (c). Vertical dashed lines mark the ice thickness and ΔH_i the change in ice thickness between both visits for the first and second strong increase in amplitude.
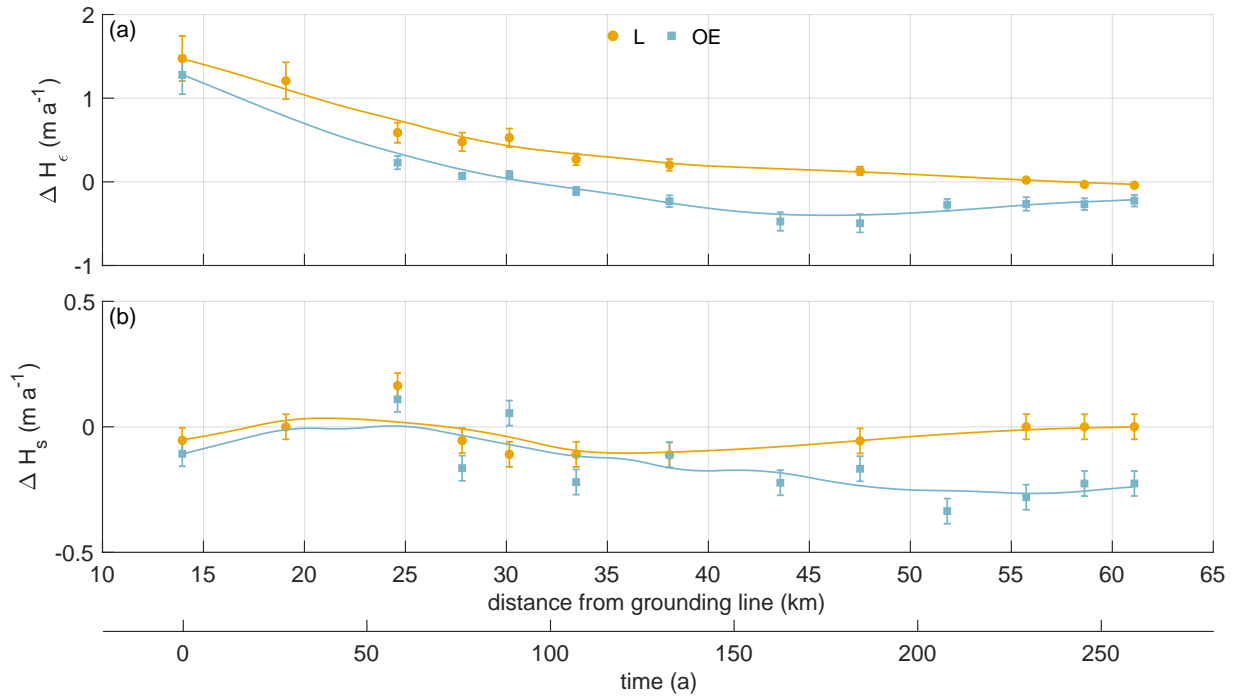
Figure A4. Distribution of pRES-derived (a) change in ice thickness due to strain and (b) ice thickness change due to surface process (firn compaction and accumulation) above the channel (yellow dots) and outside east of the channel (blue squares). The solid lines represent a smoothed fit. Error bars mark the uncertainties of the pRES-derived values.
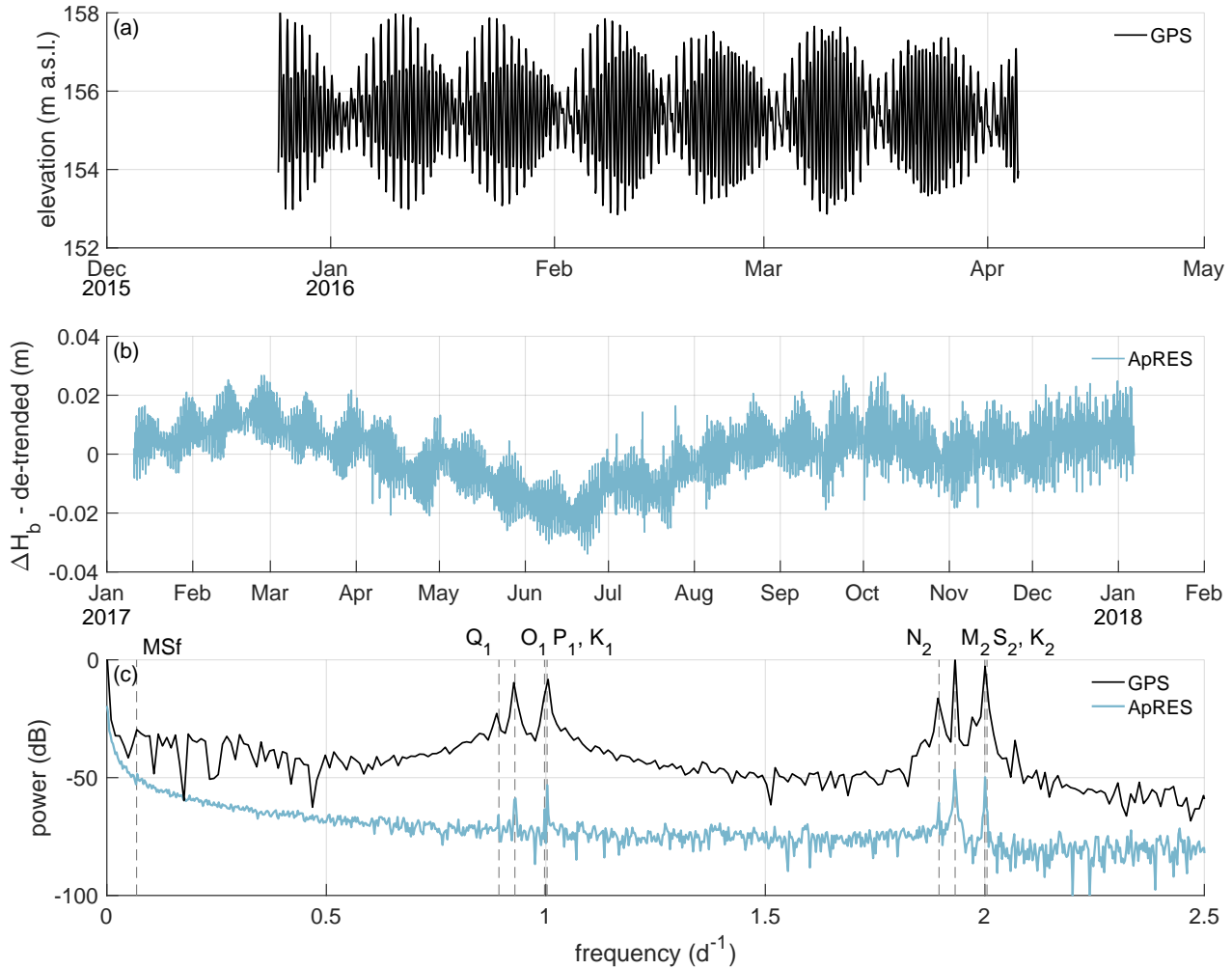
Figure A5. (a) Surface elevation recorded by the GPS station from end of December 2015 to early April 2016. (b) Linear de-trended cumulative melt (ΔH_b) from ApRES observations between January 2017 and January 2018. (c) Frequency spectrum from data shown in (a) and (b). Vertical gray dashed lines mark the constituents with half day periods ($N_2 = 12.66$ h, $M_2 = 12.42$ h, $S_2 = 12.00$ h, $K_2 = 11.97$ h), daily periods ($Q_1 = 26.87$ h, $O_1 = 25.82$ h, $P_1 = 24.07$ h, $K_1 = 23.93$ h), and Fortnightly period (MSf $= 14.76$ d). Notice, due to a shorter measuring period of the GPS, the resolution in frequency space is lower than of the ApRES.

Appendix B: Modeling

B1 Viscoelastic model for nonlinear strains

This section presents the basic equations for a viscoelastic Maxwell model applicable for finite strains. To consider finite deformations, we need to distinguish different configurations (Fig. B1). The reference configuration (stresses and strains denoted by the subscript 0) includes all positions X of material points in an initially undeformed domain. The displacement vector field $u = x - X$ relates the particle position vector X in the reference configuration to its spatial position x in the current configuration depending on the external load and the time passed (Fig. B1). To formulate differential equations for finite viscoelasticity, we focus on the system of equations with respect to the reference configuration, which is frequently applied in solid mechanics Haupt (2000).

In the reference configuration, the quasi-static momentum balance reads

$$\mathrm{Div}\,\boldsymbol{\sigma}_0 + \boldsymbol{f}_0 = \boldsymbol{0} \tag{B1}$$

with $\mathrm{Div}(\cdot)$ the divergence with respect to the reference configuration. The tensor $\boldsymbol{\sigma}_0 = J\boldsymbol{\sigma}\boldsymbol{F}^{-T}$ is the first Piola-Kirchhoff stress containing the Jacobian determinant $J = \det(\boldsymbol{F})$, the Cauchy stress $\boldsymbol{\sigma}$ of the current configuration and the transposed inverse of the deformation gradient

$$\boldsymbol{F} = \frac{\partial \boldsymbol{x}}{\partial \boldsymbol{X}} = \frac{\partial \boldsymbol{u}}{\partial \boldsymbol{X}} + \boldsymbol{I} \tag{B2}$$

characterizing the material gradient of motion in which $\boldsymbol{I}$ is the second order identity tensor. The volume force $\boldsymbol{f}_0 = -(J\rho_{\mathrm{ice}}g)\boldsymbol{e}_z$ accounts for the gravitational force in the thickness direction using the ice density $\rho_{\mathrm{ice}} = 910\,\mathrm{kg\,m^{-3}}$, the acceleration due to gravity g, and the upward pointing unit vector $\boldsymbol{e}_z = (0,0,1)^T$. The formulation for finite viscoelasticity uses the conceptual multiplicative decomposition of the deformation gradient

$$\boldsymbol{F} = \boldsymbol{F}_{\mathrm{e}}\boldsymbol{F}_{\mathrm{v}} \tag{B3}$$

into rate-independent elastic (e) and rate-dependent viscous (v) parts (Lee, 1969). All material equations are formulated in the intermediate configuration (stresses and strains denoted by $\tilde{(\cdot)}$) as an additive decomposition of the strain (similar to linearized strain; Christmann et al., 2019) is feasible in the intermediate configuration

$$\tilde{\boldsymbol{\epsilon}} = \tilde{\boldsymbol{\epsilon}}_{\mathrm{e}} + \tilde{\boldsymbol{\epsilon}}_{\mathrm{v}}. \tag{B4}$$

The elastic strain is given by $\tilde{\boldsymbol{\epsilon}}_{\mathrm{e}} = \frac{1}{2}\left(\boldsymbol{F}_{\mathrm{e}}^T\boldsymbol{F}_{\mathrm{e}} - \boldsymbol{I}\right)$ and the viscous strain by $\tilde{\boldsymbol{\epsilon}}_{\mathrm{v}} = \frac{1}{2}\left(\boldsymbol{I} - \boldsymbol{F}_{\mathrm{v}}^{-T}\boldsymbol{F}_{\mathrm{v}}^{-1}\right)$. For a viscoelastic Maxwell model, the viscous stress is equal to the elastic stress in the intermediate configuration. If we assume a Saint-Venant-Kirchhoff material for the elastic material, we get

$$\tilde{\boldsymbol{\sigma}}^D = 2\mu\tilde{\boldsymbol{\epsilon}}_{\mathrm{e}}^D = 2\eta\overset{\Delta}{\tilde{\boldsymbol{\epsilon}}}_{\mathrm{v}} \tag{B5}$$

with the viscosity η, the first Lamé constant $\mu = E/\left[2(1+\nu)\right]$ and the deviatoric part of the elastic strain $\tilde{\epsilon}_e^D = \tilde{\epsilon}_e - \frac{1}{3}\mathrm{tr}(\tilde{\epsilon}_e)\boldsymbol{I}$. The viscous strain rate is defined using the objective lower Oldroyd rate $\overset{\Delta}{\tilde{\epsilon}}_v = \dot{\tilde{\epsilon}}_v + \boldsymbol{l}_v^T \tilde{\epsilon}_v + \tilde{\epsilon}_v \boldsymbol{l}_v$ with the viscous deformation rate $\boldsymbol{l}_v = \dot{\boldsymbol{F}}_v \boldsymbol{F}_v^{-1}$ and the time derivative $\mathrm{d}(\cdot)/\mathrm{d}t$ denoted by the superimposed dot.

For the viscoelastic simulation, we have to formulate all equations and boundary conditions in the same configuration; here, we choose the reference configuration. Beside solving the momentum balance (B1), we solve the material law

$$\boldsymbol{\sigma}_0^S = \frac{\lambda + \frac{2}{3}\mu}{2}\left[\mathrm{tr}\boldsymbol{C}\boldsymbol{C}_v^{-1} - 3\right]\boldsymbol{C}_v^{-1} + \mu\left[\boldsymbol{C}_v^{-1}\boldsymbol{C}\boldsymbol{C}_v^{-1} - \frac{1}{3}\mathrm{tr}\left(\boldsymbol{C}\boldsymbol{C}_v^{-1}\right)\boldsymbol{C}_v^{-1}\right] \tag{B6}$$

with the symmetric second Piola-Kirchhoff stress $\boldsymbol{\sigma}_0^S = \boldsymbol{F}^{-1}\boldsymbol{\sigma}_0$, the second Lamé constant $\lambda = \frac{E\nu}{(1+\nu)(1-2\nu)}$ and the right Cauchy-Green tensor $\boldsymbol{C} = \boldsymbol{F}^T\boldsymbol{F}$. For a viscoelastic Maxwell material, we either have to compute elastic or viscous deformations through an internal variable in the reference configuration. The evolution equation for the internal variable $\boldsymbol{C}_v = \boldsymbol{F}_v^T\boldsymbol{F}_v$ reads

$$\eta\dot{\boldsymbol{C}}_v = \mu\left(\boldsymbol{C} - \frac{1}{3}\mathrm{tr}(\boldsymbol{C}\boldsymbol{C}_v^{-1})\boldsymbol{C}_v\right). \tag{B7}$$

At last, we have to define the boundary conditions in the reference configuration. Dirichlet conditions are the same in reference and current configuration, while traction boundary conditions change due to adjusting normal vectors for the different configurations. To model compression and extension, the horizontal displacements acting on the lateral boundaries are computed out of the observed strain at the position OE

$$u_{\text{left}} = u_x(t), \qquad u_{\text{right}} = -u_x(t) \tag{B8}$$

with u_x the displacement component in across-flow direction (Eq. 12, Fig. 5). The upper surface is traction-free and the base perceive the depth-increasing water pressure of the current configuration

$$p = \begin{cases} \rho_{\text{sw}}g(-z - u_z) & \text{for } z + u_z \le 0 \\ 0 & \text{else} \end{cases} \tag{B9}$$

in normal direction with sea water density $\rho_{\text{sw}} = 1028\,\mathrm{kg\,m^{-3}}$ and u_z the displacement component in the thickness direction. Hence, we have to compute the water pressure in the reference configuration

$$\boldsymbol{t}_0 = P_0\boldsymbol{N} = pJ\boldsymbol{F}^{-T}\boldsymbol{N} = p\boldsymbol{n} \tag{B10}$$

with the pressure P_0 and the normal vector $\boldsymbol{N}$ in the reference configuration as well as the pressure p and the normal vector $\boldsymbol{n}$ in the current configuration. Additionally, we deform the geometry by temporally and spatially variable fields of basal melt subtracted at the lower boundary and SMB added to the upper boundary.

B2 Viscosity from inverse modeling

For estimating the viscosity distribution in the Filchner-Ronne Ice Shelf, we conduct a control-method inversion for the rheology parameter in the floating part using a non-Newtonian rheology with $n = 3$. By this we mean that we invert for the
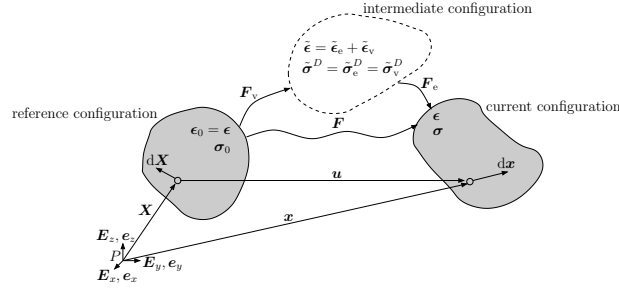
Figure B1. Reference, current and intermediate configurations and their corresponding strain and stress denotation for the finite viscoelastic Maxwell model. In the intermediate configuration (dashed line) the viscoelastic material equations are defined.

ice-stiffness parameter B, more accurately for the vertically averaged rheology $\bar{B}$. We use the Ice Sheet and Sea Level System Model (Larour et al., 2012) applied to the Filchner-Ronne Ice Shelf using the Blatter-Pattyn higher-order approximation (Blatter, 1995; Pattyn, 2003). The calculation is done on an unstructured finite element grid with a refined resolution of $2\,\mathrm{km}$ at the grounding line, in the shear margins as well as at other regions of faster ice flow. In the melt channel domain we further refine the resolution of the grid to $0.5\,\mathrm{km}$.

To generate the geometry of the ice shelf the BedMachine Antarctica v2 data set is used (Morlighem et al., 2020; Morlighem, 2020). For the ice rigidity in the grounded region, as well as an initial guess of ice rigidity in the floating shelf, we assume the results of a long-term thermal spin-up also used in Eisen et al. (2020) based on the geothermal flux from Martos et al. (2017). We set Glen's flow-law exponent to $n = 3$ and the viscosity η is described by the Cuffey-Temperate rheology law provided by ISSM. We constrain ice surface velocities to fit the MEaSUREs data set (Mouginot et al., 2019b, a).

Our optimization approach infers iteratively two parameters – the basal friction parameter k in the grounded area based on a linear sliding law and the ice vertically averaged rheology parameter $\bar{B}$ in the floating area. For this purpose two cost functions are built. Each cost function consists of two at the surface S evaluated data misfits, linear and logarithmic, as well as a Tikhonov regularization term:

$$J(\boldsymbol{v},p) = \gamma_1 \int\limits_S \frac{(v_x - v_x^{\mathrm{obs}})^2 + (v_y - v_y^{\mathrm{obs}})^2}{2}\,\mathrm{d}S + \gamma_2 \int\limits_S \left(\log\left(\frac{||\boldsymbol{v}|| + \xi}{||\boldsymbol{v}^{\mathrm{obs}}|| + \xi} \right) \right)^2 \mathrm{d}S + \gamma_t\, J_{\mathrm{reg}}(p) \tag{B11}$$

with $\boldsymbol{v}^{\mathrm{obs}}$ the observed surface velocity, $\boldsymbol{v}$ the modeled velocity, $p = \{k, \bar{B}\}$ the respective control parameter for the inversion and a added minimal velocity ξ to avoid singularities. The first term will be most sensitive to velocity observations in fast-flowing areas, the second term will be most sensitive to velocity observations in slow-floating areas, while the third term $J_{\mathrm{reg}}(p)$ penalizes oscillations in the optimization parameter p. We performed an L-curve analysis to find suitable weights $\gamma_1, \gamma_2, \gamma_t$ for both cost functions. With this trade-off curve, we can make sure that we find a regularization term that fits the data well without overfitting noise. For the basal friction inversion, we found best weights $\gamma_1 = 1$, $\gamma_2 = 5 \times 10^{-6}$ and $\gamma_t = 1 \times 10^{-8}$, while for the ice rigidity inversion the optimal weights were $\gamma_1 = 1, \gamma_2 = 0.8$ and $\gamma_t = 4 \times 10^{-17}$.

We linearize and solve the optimization problem using the M1QN3 algorithm with an incomplete adjoint (Larour et al., 2012).

For this inversion setting we apply a gradient relative convergence criterion $\varepsilon_{\mathrm{gttol}} = 10^{-6}$ and two points which are less then $\mathrm{dxmin} = 10^{-4}$ from each other are considered identical. Besides we use a maximum number of iterations and function evaluations of 1000.

With the help of Glen's flow law the resulting rheology parameter $\bar{B}$ from the inversion is used for calculating the effective viscosity

$$\eta = \frac{\bar{B}}{2\dot{\varepsilon}_e^{\frac{1-n}{n}}} \tag{B12}$$

where $\dot{\varepsilon}_e$ describes the effective strain rate. We show our best-fit results for ice viscosity in the region around the melt channel in Fig. B2. The range of the vertically averaged viscosity is between 5.0563×10^{13} and $2.6656 \times 10^{15}\,\mathrm{Pa\,s}$.
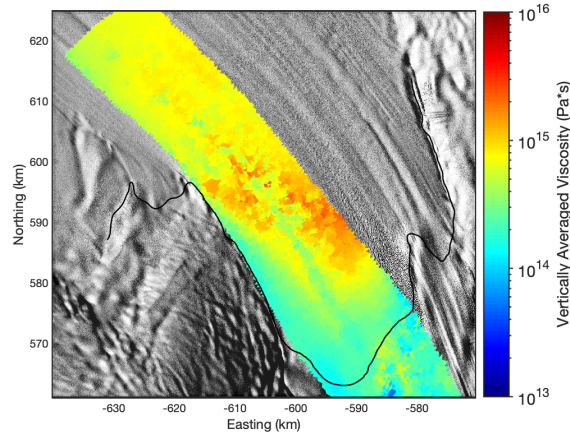
Figure B2. Ice viscosity in the melt channel area obtained from inverse modeling. The map extent is the same as in Fig. 1. The background image is a hillshade of the Reference Elevation Model of Antarctica (Howat et al., 2018, 2019).

B3 Sensitivity of experiment 2 on viscosity

To capture the influence of the viscosity, different constant values (one smaller and one higher as in the second experiment) are investigated in a further experiment. The spin-up for each viscosity starts at $t = -75\,\mathrm{a}$ with a basal geometry that should fit seismic IV profile at the end of the spin-up (t_0). The melt rate $a_b^{\mathrm{syn}}(t_0)$ is again assumed to be constant over the spin-up for all different viscosity values. We force the base with the synthetic melt rate (Fig. 3a), the same melt rate we already used in the second experiment. The initial base (at $t = -75\,\mathrm{a}$) for the middle and high viscosity is nearly the same as $5 \times 10^{15}\,\mathrm{Pa\,s}$ is for ice a rather high value requiring cold ice (Fig. B8). For the smallest viscosity, a deeper channel at the beginning of the spin-up is needed.

B4 Elastic strain measure

For the concept of nonlinear strain, strain measures are defined and valid in particular configurations. However, the commonly used strain measures, like the Green-Lagrange strain in the reference configuration or the Euler-Almansi strain in the actual configuration, always have combined viscoelastic parts that cannot be split into viscous and elastic parts separately due to the multiplicative decomposition of the deformation gradient (Eq. B3). To quantify the elastic contribution of the melt channel evolution, we consider the Hencky strain, often called true strain, a logarithmic strain measure introduced in more detail by (Cuitino and Ortiz, 1992). Xiao (2005) and Neff et al. (2015) showed an extensive overview of the logarithmic strain properties and its applications. The advantage of the Hencky strain is an additive decomposition of the strain into an elastic and viscous part comparable to the procedure assuming a linearized strain for the linear strain theory. Furthermore, the Hencky strain is identical in the reference and current configuration.

The Hencky strain is defined by

$$\epsilon^H = \frac{1}{2}\ln(\boldsymbol{F}^T\boldsymbol{F}) = \frac{1}{2}\ln(\boldsymbol{C}). \tag{B13}$$

We can compute the logarithm of the right Cauchy- Green tensor $\boldsymbol{C}$ by logarithmizing the eigenvalues derived by a spectral decomposition. For rigid body motions when $\boldsymbol{C} = \boldsymbol{I}$, the Hencky strain is zero. The eigenvalues of $\boldsymbol{F}^T\boldsymbol{F}$ for the Lagrangian perspective are the same as the eigenvalues of $\boldsymbol{F}\boldsymbol{F}^T$ in the Eulerian sense. Hence, the Hencky strain in the reference configuration is the same as in the current configuration and, for simplicity, we call it strain ϵ here.

In the viscoelastic Maxwell model considering finite strains, we have a multiplicative decomposition of the deformation gradient $\boldsymbol{F}$ in an elastic and viscous part (Eq. B3) and it holds

$$\boldsymbol{C} = \boldsymbol{F}^T\boldsymbol{F} = \boldsymbol{F}_v^T\boldsymbol{F}_e^T\boldsymbol{F}_e\boldsymbol{F}_v = \boldsymbol{F}_v^T\boldsymbol{C}_e\boldsymbol{F}_v \tag{B14}$$

with $\boldsymbol{C}_e = \boldsymbol{F}_e^T\boldsymbol{F}_e$. Furthermore, we can split the deformation gradient in a rotation $\boldsymbol{R}$ and a stretching $\boldsymbol{U}$ ($\boldsymbol{F} = \boldsymbol{R}\boldsymbol{U}$). The rotation has to be orthogonal, hence, we arbitrarily choose the viscous rotation as the identity tensor ($\boldsymbol{R}_v = \boldsymbol{I}$) and get

$$\boldsymbol{C} = \boldsymbol{U}_v^T\boldsymbol{C}_e\boldsymbol{U}_v \quad \Rightarrow \quad \ln(\boldsymbol{C}) = \ln(\boldsymbol{U}_v^T) + \ln(\boldsymbol{C}_e) + \ln(\boldsymbol{U}_v). \tag{B15}$$

The stretching is symmetric ($\boldsymbol{U}_v^T = \boldsymbol{U}_v$) and we get $2\ln(\boldsymbol{U}_v) = \ln(\boldsymbol{U}_v^2) = \ln(\boldsymbol{C}_v)$ based on the relation $\boldsymbol{C}_v = \boldsymbol{U}_v^2$. In the end, we can split the strain additive into

$$\underbrace{\ln(\boldsymbol{C})}_{2\epsilon} = \underbrace{\ln(\boldsymbol{C}_e)}_{2\epsilon^e} + \underbrace{\ln(\boldsymbol{C}_v)}_{2\epsilon^v} \tag{B16}$$

and get the elastic strain

$$\epsilon^e = \epsilon - \epsilon^v = \frac{1}{2}\ln(\boldsymbol{C}) - \frac{1}{2}\ln(\boldsymbol{C}_v), \tag{B17}$$

where $\boldsymbol{C}_v$ is the internal variable of the viscoelastic material model.
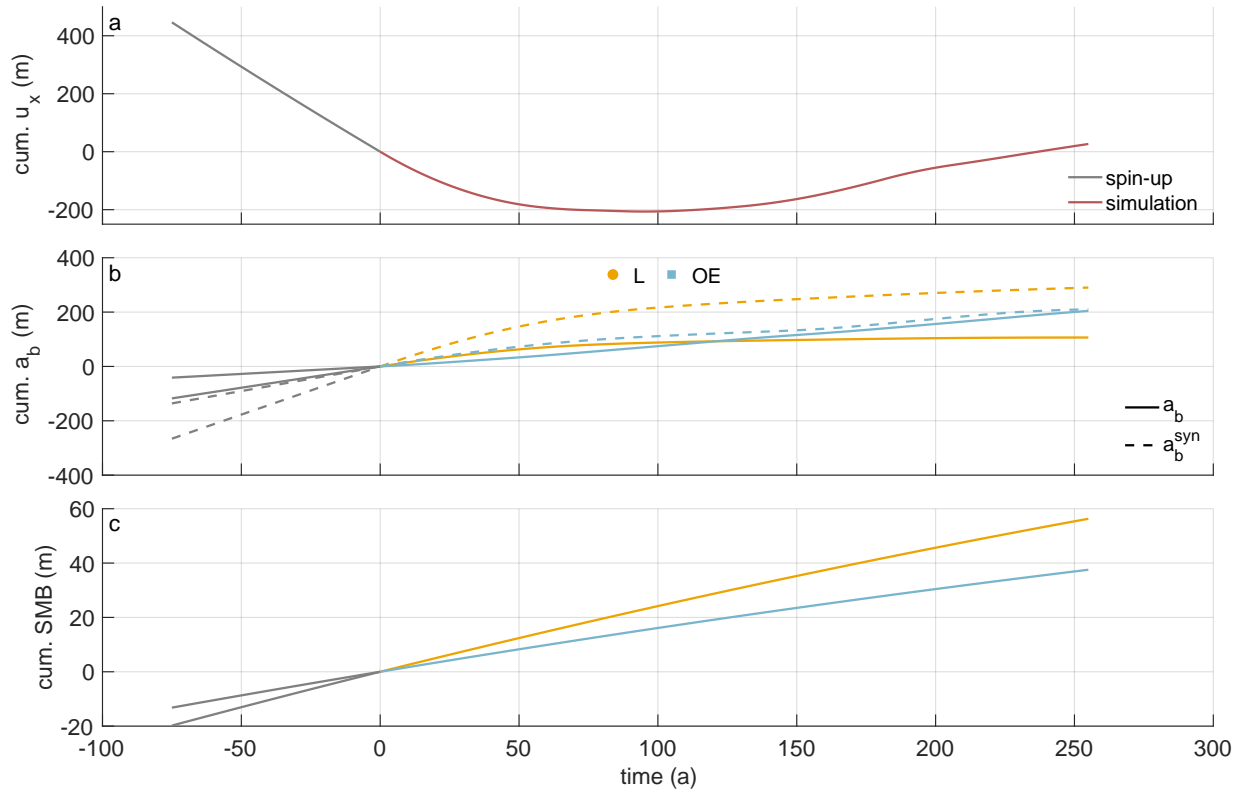
Figure B3. Model input derived from pRES measurements and RACMO (van Wessem et al., 2014). (a) Cumulative horizontal displacement of the lateral boundaries calculated from pRES-derived vertical strain rates outside of the channel. (b) Cumulative basal melt rates above (yellow) and outside the channel (blue). Solid lines are derived from the pRES measurements and dashed lines are synthetic melt rates that are necessary to reproduce the measured ice thickness distribution. (c) Cumulative surface mass balance (SMB) derived from multi-year mean RACMO2.3 data (van Wessem et al., 2014) for a density of $910\,\mathrm{kg\,m^{-3}}$ outside the channel (blue) and above the channel (yellow), 50% larger. Gray lines represent values used in the spin-up and colored lines values used in the simulation of the evolution of the channel.
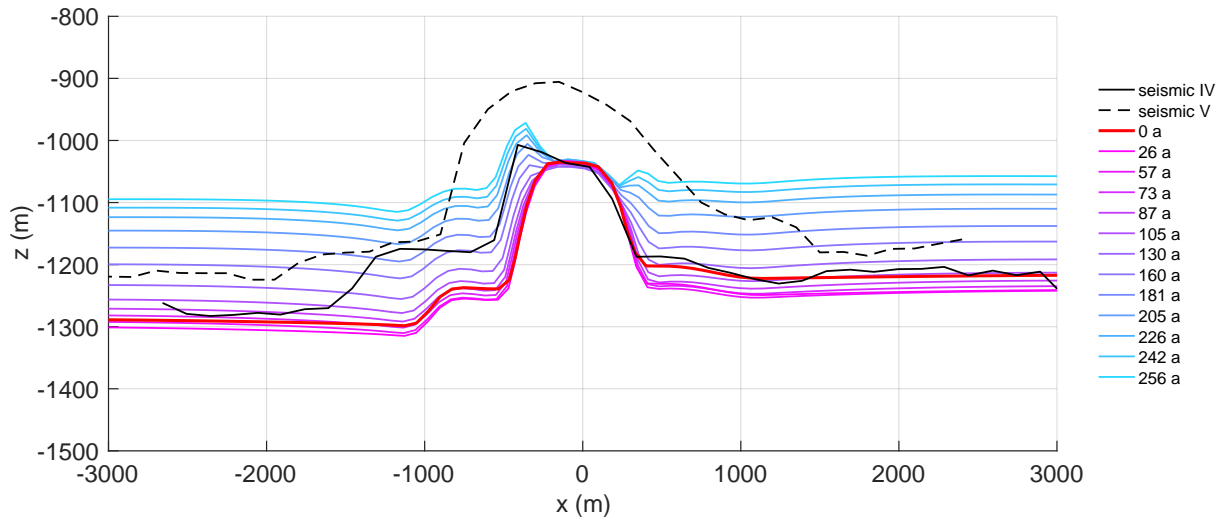
Figure B4. Evolution of the base for the first experiment applying pRES-derived melt rates in the viscoelastic simulation. The black curve shows seismic profile IV (Hofstede et al., 2021b) and the red line the simulated base after the spin-up. For each position of pRES observations, the simulated base is shown using a color distribution ranging from red (furthest upstream) to blue (furthest downstream). The dashed black line is the base of seismic profile V (Hofstede et al., 2021b) near the pRES observation fitting to 130 a
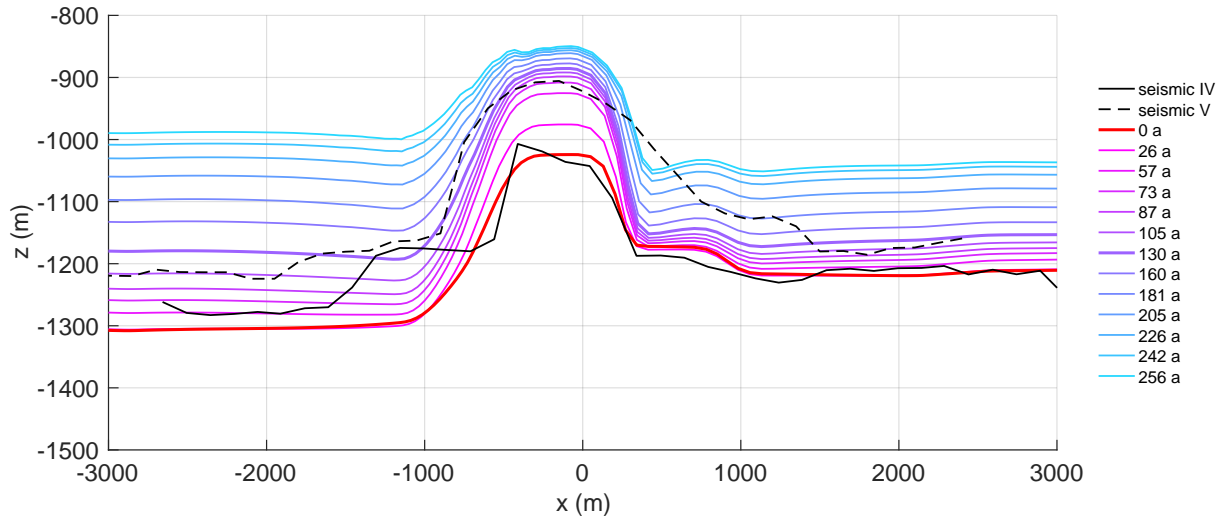
Figure B5. Evolution of the base for the second experiment applying synthetic melt rates in the viscoelastic simulation.The black curve shows seismic profile IV (Hofstede et al., 2021b) and the red line is the simulated base after the spin-up. For each position of pRES observations, the simulated base is shown using a color distribution ranging from red (furthest upstream) to blue (furthest downstream). The dashed black line is the base of seismic profile V (Hofstede et al., 2021b) near the pRES observation fitting to $130\,a$. The opening of the basal channel cannot be rebuilt with the model as the melt rate inside the channel is only applied to constant channel width. The basal channel stays open during the simulation time of $256\,a$.
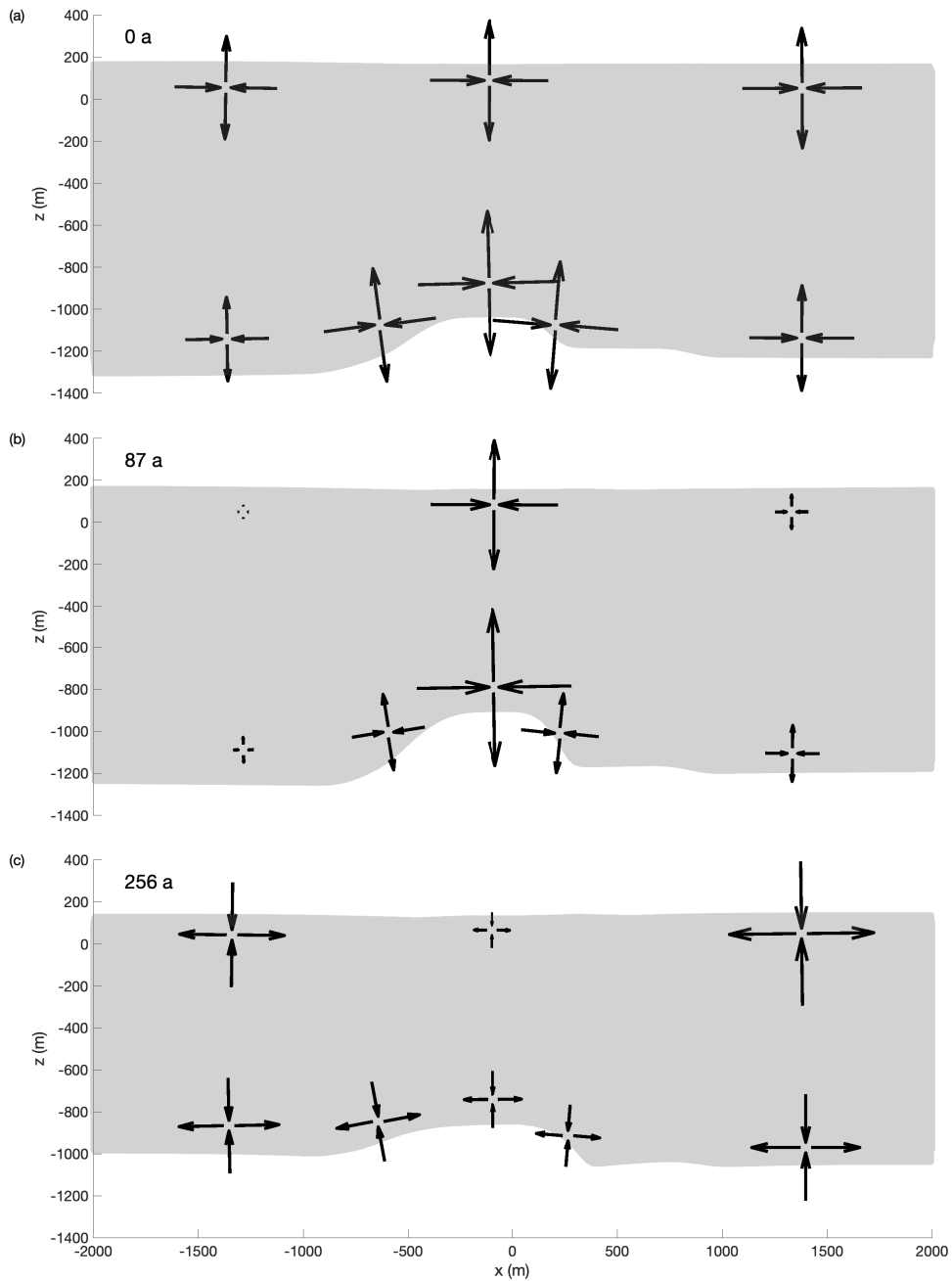
Figure B6. Schematic arrows with their length according to the simulated principal strain magnitude and the pointing direction fitting to principal strain directions at specific points in the cross section for three different points in time (a) at $t = 0\,\mathrm{a}$ (after the spinup, maximum lateral compression), (b) $t = 87\,\mathrm{a}$ (small lateral displacement), (c) $t = 256\,\mathrm{a}$ (end of the simulation).
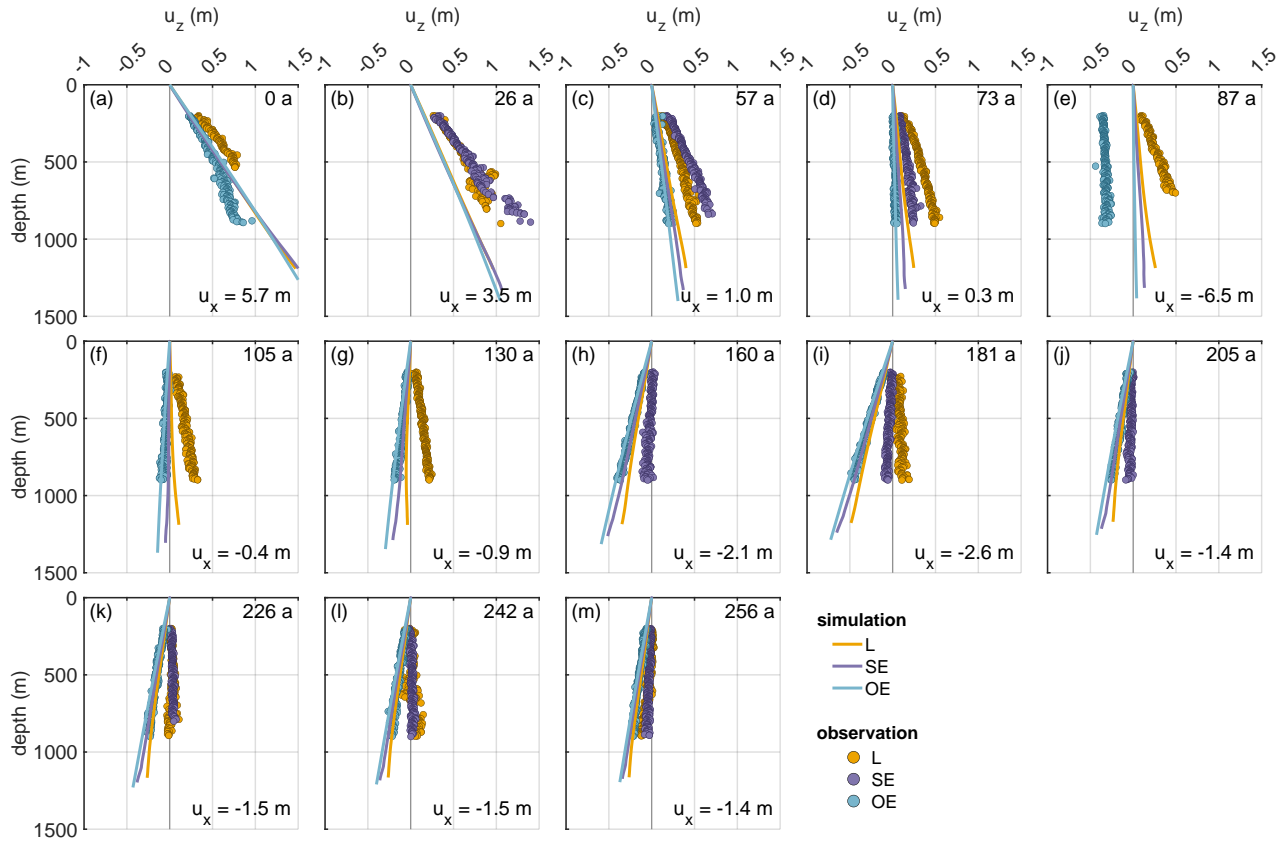
Figure B7. First experiment: comparison of displacements (u_z) derived from pRES measurements (dots) and from the simulations (lines). The different panels show the displacement for $\Delta t = 1\,\mathrm{a}$ allocated to the year of the model (number in upper right corner). The numbers in the lower right corners give horizontal displacement u_x derived from ε_{zz} of the pRES measurements outside the channel (OE) with positive values representing compression and negative values extension.
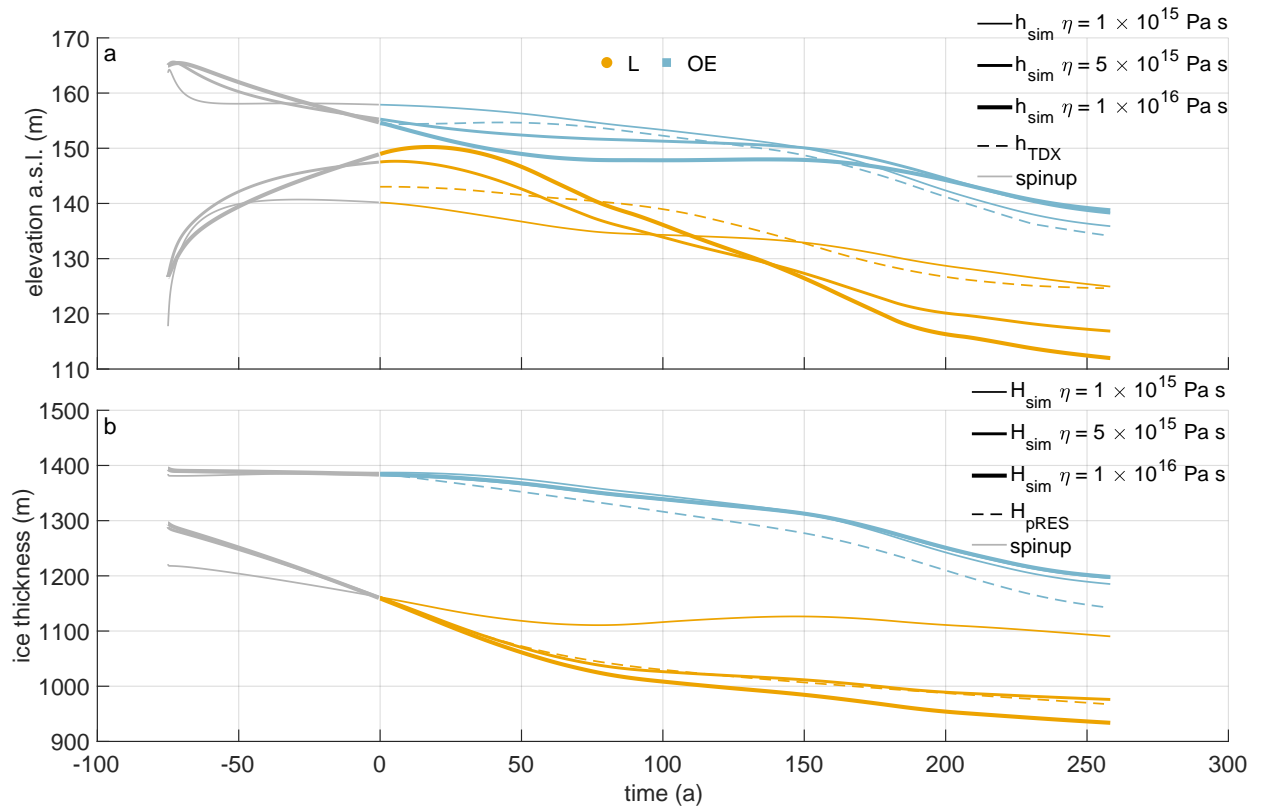
Figure B8. (a) Surface elevation above the channel (yellow) and outside the channel (blue) derived from the simulation (solid lines) and from TanDEM-X DLR (2020) (dashed lines). (b) Ice thickness above the channel (yellow) and outside the channel (blue) derived from the simulation (solid lines) and from pRES measurements (dashed lines). The thickness of the solid lines represents the different viscosities: $1 \times 10^{15}\,\mathrm{Pa\,s}$ (thin line), $5 \times 10^{15}\,\mathrm{Pa\,s}$ (medium line, same value as in the second experiment), $1 \times 10^{16}\,\mathrm{Pa\,s}$ (thick line). Gray lines represent values used in the spin-up and colored lines values used in the simulation of the evolution of the channel.
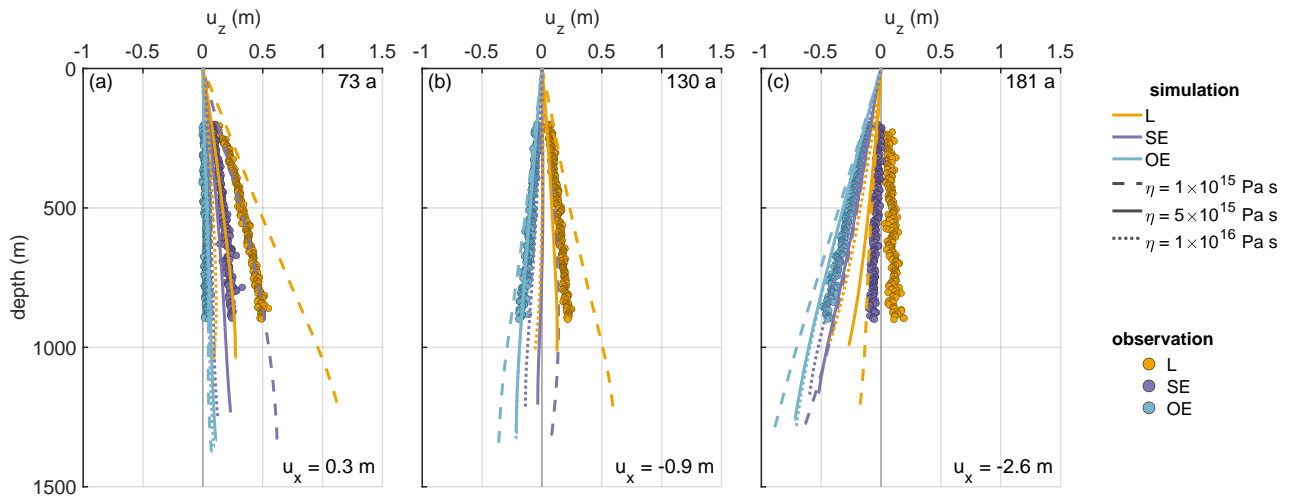
Figure B9. Second experiment: comparison of displacements (u_z) derived from observations (dots) and the simulations for different viscosities displayed by different line styles (lines). The different panels show the displacement for $\Delta t = 1\,\mathrm{a}$ allocated to the simulation time (upper right corner). The numbers in the lower right corners give horizontal displacement u_x derived from ε_{zz} of the pRES measurements outside the channel (OE) with positive values representing compression and negative values extension.
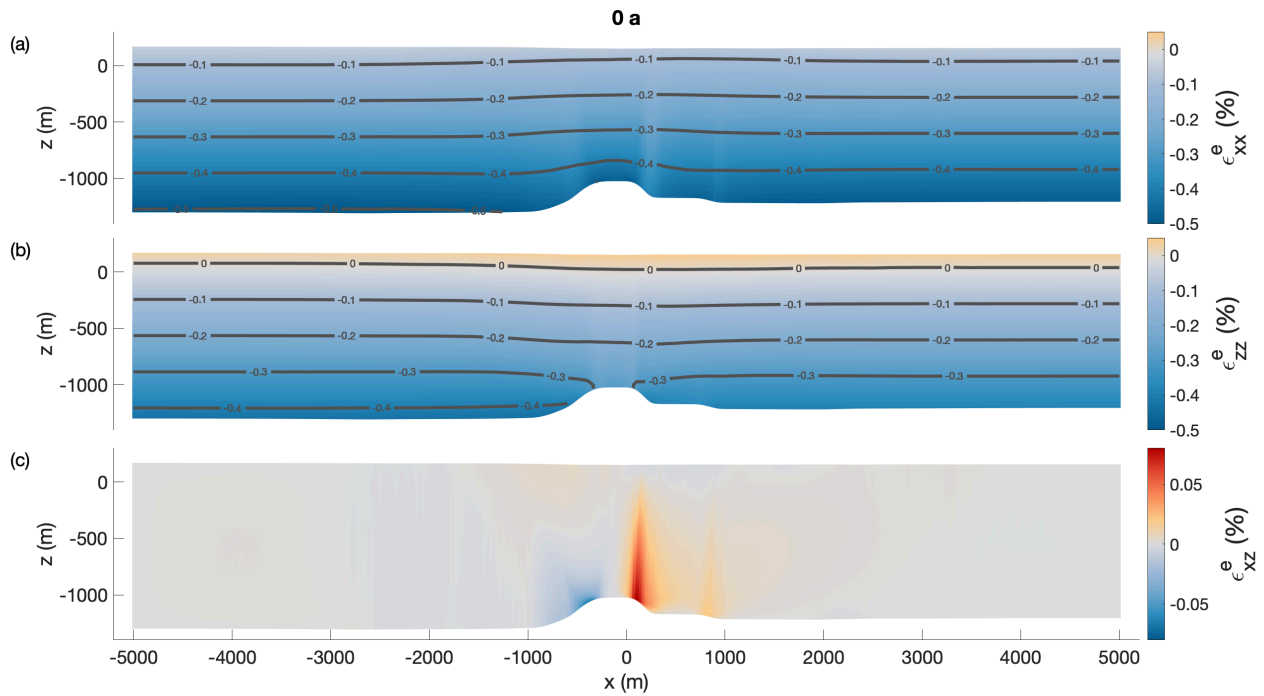
Figure B10. The simulated elastic part of Hencky strain (a) in across-flow direction, (b) in vertical direction and (c) the shear component for the second experiment using synthetic melt rates at $t = 0\,\mathrm{a}$ (after the spin-up, maximum lateral compression). The gray lines are contour lines of the elastic strain components. The normal components reach permille values (the blueish colors denote compression), while the shear component is one order of magnitude smaller.
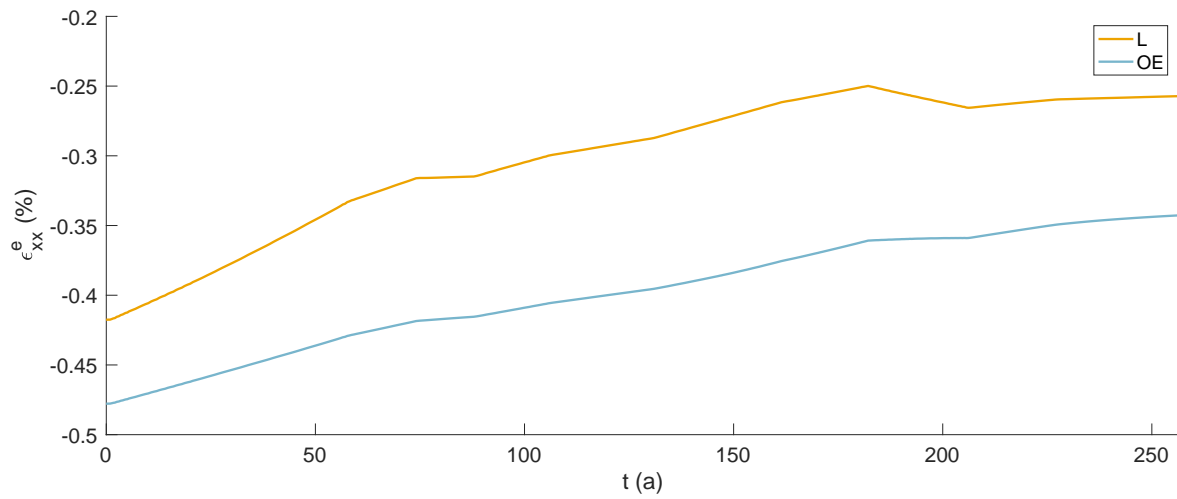
Figure B11. The evolution of the simulated elastic part of Hencky strain at the ice base inside and outside east the channel in percent over the simulation time of $256\,\mathrm{a}$. The initial elastic response of the grounded ice becoming afloat has vanished as the grounding line to far upstream. The spinup of $75\,\mathrm{a}$ leads to a continuous elastic transition at $t = 0\,\mathrm{a}$ the start of the comparison between simulated results and observations.
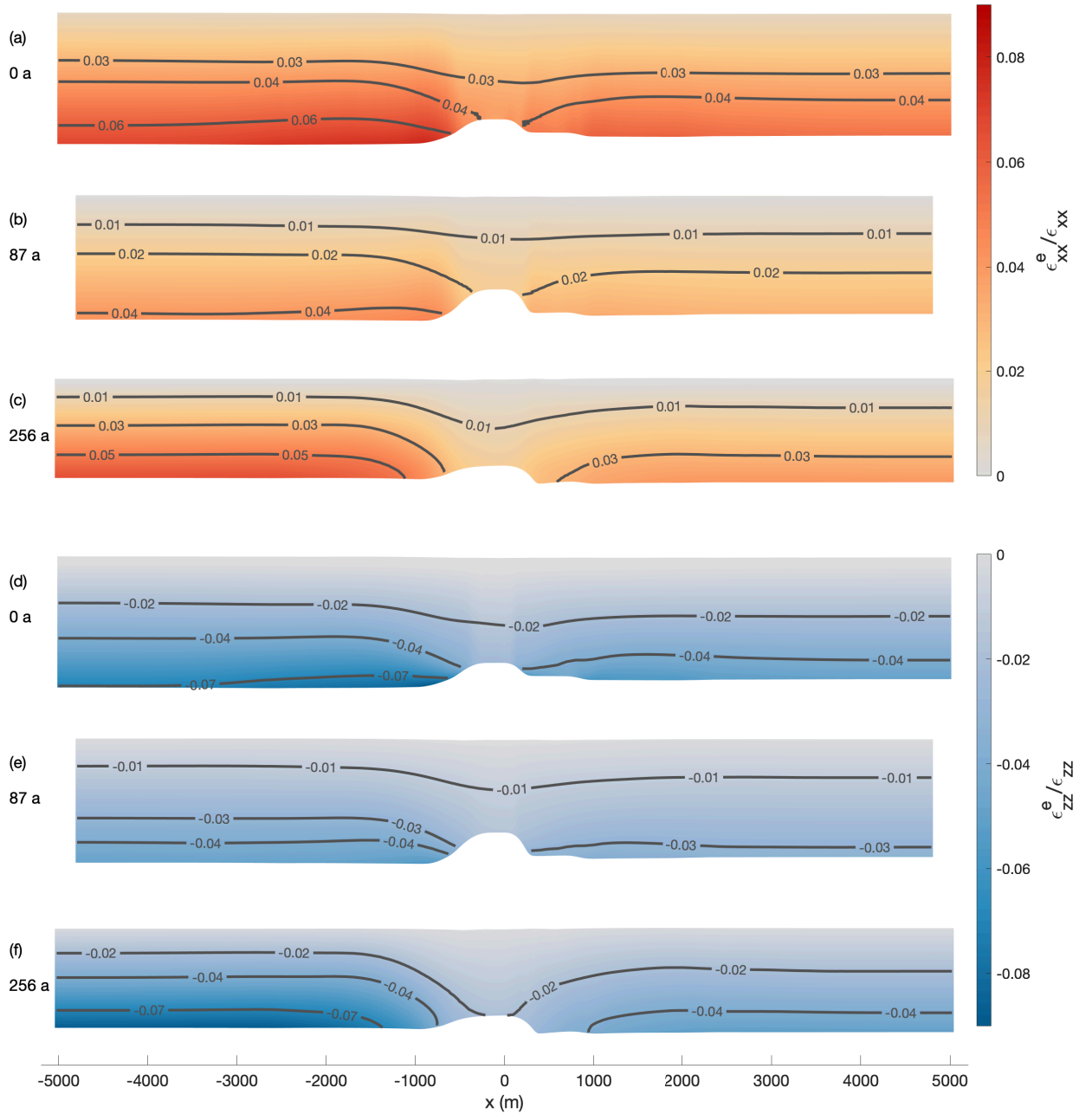
Figure B12. Relative contribution of elastic to total strain of the second experiment using synthetic melt rates for the simulation. The upper three panels show the relative elastic strain in across-flow direction $\epsilon_{xx}^e/\epsilon_{xx}$ for (a) $t = 0\,\mathrm{a}$ (after the spin-up, maximum lateral compression), (b) $t = 87\,\mathrm{a}$ (small lateral displacement), (c) $t = 256\,\mathrm{a}$ (end of the simulation). The lower three panels show the relative elastic strain in thickness direction $\epsilon_{zz}^e/\epsilon_{zz}$ for (d) $t = 0\,\mathrm{a}$ (after the spin-up, maximum lateral compression), (e) $t = 87\,\mathrm{a}$ (small lateral displacement), (f) $t = 256\,\mathrm{a}$ (end of the simulation). The negative values denote that the elastic and viscous strains have different signs. The elastic and viscous Hencky strain sum up to the total strain.

Author contributions. AH has designed the study, conducted the field study together with DS and wrote the manuscript together with OZ, JC, KWN, VH and LH. OZ processed the pRES/ApRES data and analyzed the melt rates together with AH. JC performed the viscoelastic simulations together with TS and with contributions from OZ and AH. JC, AH and OZ analyzed the results together with RM. VH and OZ processed the GPS data. LH and MW performed the inverse modeling. CH performed the seismic measurements and supported the

745   discussions. NN calculated the TDX-DEM. KWN supported the field study and contributed to melt rate analysis and its discussion together with HFJC. All authors helped to improve writing.

Competing interests. The authors declare that they have no conflict of interest.

Acknowledgements. This work was funded by the AWI strategy fund project FISP. We acknowledge the support of BAS for the field campaign, in particular the support of the Graham Niven and Bradley Morell, who have been field assistants in the two expeditions. L.H. is

750   funded through the Helmholtz School for Marine Data Science (MarDATA), Grant No. HIDSS-0005. Support for this work came from the UK Natural Environment Research Council large grant "Ice shelves in a warming world: Filchner Ice Shelf System" (NE/L013770/1).

References

Alley, K. E., Scambos, T. A., Alley, R. B., and Holschuh, N.: Troughs developed in ice-stream shear margins precondition ice shelves for ocean-driven breakup, Science Advances, 5, eaax2215, https://doi.org/10.1126/sciadv.aax2215, 2019.

755 Bassis, J. and Ma, Y.: Evolution of basal crevasses links ice shelf stability to ocean forcing, Earth and Planetary Science Letters, 409, 203–211, https://doi.org/https://doi.org/10.1016/j.epsl.2014.11.003, 2015.

Blatter, H.: Velocity and stress fields in grounded glaciers: a simple algorithm for including deviatoric stress gradients, Journal of Glaciology, 41, 333–344, https://doi.org/10.3189/S002214300001621X, 1995.

Brennan, P. V., Lok, L. B., Nicholls, K., and Corr, H.: Phase-sensitive FMCW radar system for high-precision Antarctic ice shelf profile
760 monitoring, IET Radar, Sonar & Navigation, 8, 776–786, https://doi.org/10.1049/iet-rsn.2013.0053, 2014.

Christmann, J., Plate, C., Müller, R., and Humbert, A.: Viscous and viscoelastic stress states at the calving front of Antarctic ice shelves, Annals of Glaciology, 57, 10–18, https://doi.org/10.1017/aog.2016.18, 2016.

Christmann, J., Müller, R., and Humbert, A.: On nonlinear strain theory for a viscoelastic material model and its implications for calving of ice shelves, Journal of Glaciology, 65, 212–224, https://doi.org/10.1017/jog.2018.107, 2019.

765 Christmann, J., Helm, V., Khan, S. A., Kleiner, T., Müller, R., Morlighem, M., Neckel, N., Rückamp, M., Steinhage, D., Zeising, O., and Humbert, A.: Elastic deformation plays a non-negligible role in Greenland's outlet glacier flow, Communications Earth & Environment, 2, 232, https://doi.org/10.1038/s43247-021-00296-3, 2021.

Corr, H. F., Jenkins, A., Nicholls, K. W., and Doake, C.: Precise measurement of changes in ice-shelf thickness by phase-sensitive radar to determine basal melt rates, Geophysical Research Letters, 29, 73–1 73–4, https://doi.org/10.1029/2001GL014618, 2002.

770 Cuitino, A. and Ortiz, M.: Computational modelling of single crystals, Modelling and Simulation in Materials Science and Engineering, 1, 225–263, https://doi.org/10.1088/0965-0393/1/3/001, 1992.

Dinniman, M. S., Asay-Davis, X. S., Galton-Fenzi, B. K., Holland, P. R., Jenkins, A., and Timmermann, R.: Modeling Ice Shelf/Ocean Interaction in Antarctica: A Review, Oceanography, 29, 144–153, https://doi.org/10.5670/oceanog.2016.106, 2016.

DLR: TanDEM-X - PolarDEM - Antarctica, 90m, https://doi.org/10.15489/9jhr18jepi65, 2020.

775 Dow, C. F., Lee, W. S., Greenbaum, J. S., Greene, C. A., Blankenship, D. D., Poinar, K., Forrest, A. L., Young, D. A., and Zappa, C. J.: Basal channels drive active surface hydrology and transverse ice shelf fracture, Science Advances, 4, https://doi.org/10.1126/sciadv.aao7212, 2018.

Drews, R.: Evolution of ice-shelf channels in Antarctic ice shelves, The Cryosphere, 9, 1169–1181, https://doi.org/10.5194/tc-9-1169-2015, 2015.

780 Drews, R., Pattyn, F., Hewitt, I. J., Ng, F. S. L., Berger, S., Matsuoka, K., Helm, V., Bergeot, N., Favier, L., and Neckel, N.: Actively evolving subglacial conduits and eskers initiate ice shelf channels at an Antarctic grounding line, Nature Communications, 8, 15 228, https://doi.org/10.1038/ncomms15228, 2017.

Dutrieux, P., Stewart, C., Jenkins, A., Nicholls, K. W., Corr, H. F., Rignot, E., and Steffen, K.: Basal terraces on melting ice shelves, Geophysical Research Letters, 41, 5506–5513, https://doi.org/10.1002/2014GL060618, 2014.

785 Eisen, O., Winter, A., Steinhage, D., Kleiner, T., and Humbert, A.: Basal roughness of the East Antarctic Ice Sheet in relation to flow speed and basal thermal state, Annals of Glaciology, 61, 162–175, https://doi.org/10.1017/aog.2020.47, 2020.

Foerste, C., Bruinsma, S., Abrykosov, O., Lemoine, J.-M., Marty, J. C., Flechtner, F., Balmino, G., Barthelmes, F., and Biancale, R.: EIGEN-6C4 The latest combined global gravity field model including GOCE data up to degree and order 2190 of GFZ Potsdam and GRGS Toulouse, https://doi.org/10.5880/icgem.2015.1, 2014.

790 Fujita, S., Matsuoka, T., Ishida, T., Matsuoka, K., and Mae, S.: A summary of the complex dielectric permittivity of ice in the megahertz range and its applications for radar sounding of polar ice sheets, in: Physics of ice core records, pp. 185–212, Hokkaido University Press, 2000.

Galton-Fenzi, B. K., Hunter, J. R., Coleman, R., Marsland, S. J., and Warner, R. C.: Modeling the basal melting and marine ice accretion of the Amery Ice Shelf, Journal of Geophysical Research: Oceans, 117, https://doi.org/10.1029/2012JC008214, 2012.

795 Gladish, C. V., Holland, D. M., Holland, P. R., and Price, S. F.: Ice-shelf basal channels in a coupled ice/ocean model, Journal of Glaciology, 58, 1227–1244, https://doi.org/10.3189/2012JoG12J003, 2012.

Gudmundsson, H.: Ice-stream response to ocean tides and the form of the basal sliding law, The Cryosphere, 5 (1), 259–270, https://doi.org/10.5194/tc-5-259-2011, 2011.

Gwyther, D. E., Kusahara, K., Asay-Davis, X. S., Dinniman, M. S., and Galton-Fenzi, B. K.: Vertical processes and resolution impact ice shelf basal melting: A multi-model study, Ocean Modelling, 147, 101 569, https://doi.org/10.1016/j.ocemod.2020.101569, 2020.

800 Haupt, P.: Continuum Mechanics and Theory of Materials, Springer, Berlin, https://doi.org/10.1007/978-3-662-04775-0, 2000.

Helm, V., Humbert, A., and Miller, H.: Elevation and elevation change of Greenland and Antarctica derived from CryoSat-2, The Cryosphere, 8, 1539–1559, https://doi.org/10.5194/tc-8-1539-2014, 2014.

Herron, M. M. and Langway, C. C.: Firn densification: an empirical model, Journal of Glaciology, 25, 373–385, https://doi.org/10.3189/S0022143000015239, 1980.

805 Hofstede, C., Beyer, S., Corr, H., Eisen, O., Hattermann, T., Helm, V., Neckel, N., Smith, E. C., Steinhage, D., Zeising, O., and Humbert, A.: Evidence for a grounding line fan at the onset of a basal channel under the ice shelf of Support Force Glacier, Antarctica, revealed by reflection seismics, The Cryosphere, 15, 1517–1535, https://doi.org/10.5194/tc-15-1517-2021, 2021a.

Hofstede, C., Beyer, S., Corr, H. F. J., Eisen, O., Hattermann, T., Helm, V., Neckel, N., Smith, E. C., Steinhage, D., Zeising, O., and Humbert, A.: Seismic reflection data of a basal channel and ocean cavity at the ice shelf-grounding line area of Support Force Glacier, Filchner Ice Shelf, Antarctica, https://doi.org/10.1594/PANGAEA.932278, 2021b.

810

Holland, D. M. and Jenkins, A.: Modeling Thermodynamic Ice–Ocean Interactions at the Base of an Ice Shelf, Journal of Physical Oceanography, 29, 1787 – 1800, https://doi.org/10.1175/1520-0485(1999)029<1787:MTIOIA>2.0.CO;2, 1999.

Holland, P. R. and Kwok, R.: Wind-driven trends in Antarctic sea-ice drift, Nature Geoscience, 5, 872–875, https://doi.org/10.1038/ngeo1627, 2012.

815

Howat, I., Morin, P., Porter, C., and Noh, M.-J.: The Reference Elevation Model of Antarctica, https://doi.org/10.7910/DVN/SAIK8B, 2018.

Howat, I., Porter, C., Smith, B. E., Noh, M.-J., and Morin, P.: The Reference Elevation Model of Antarctica, The Cryosphere, 13, 665–674, https://doi.org/10.5194/tc-13-665-2019, 2019.

Humbert, A., Steinhage, D., Helm, V., Hoerz, S., Berendt, J., Leipprand, E., Christmann, J., Plate, C., and Müller, R.: On the link between surface and basal structures of the Jelbart Ice Shelf, Antarctica, Journal of Glaciology, 61, 975–986, https://doi.org/10.3189/2015JoG15J023, 2015.

820

Humbert, A., Steinhage, D., Helm, V., Beyer, S., and Kleiner, T.: Missing evidence of widespread subglacial lakes at Recovery Glacier, Antarctica, Journal of Geophysical Research: Earth Surface, 123, 2802–2826, https://doi.org/10.1029/2017JF004591, 2018.

Jenkins, A. and Doake, C.: Ice-ocean interaction on Ronne Ice Shelf, Antarctica, Journal of Geophysical Research: Oceans, 96, 791–813, https://doi.org/10.1029/90JC01952, 1991.

Jenkins, A., Corr, H. F., Nicholls, K. W., Stewart, C. L., and Doake, C. S.: Interactions between ice and ocean observed with phase-sensitive radar near an Antarctic ice-shelf grounding line, Journal of Glaciology, 52, 325–346, https://doi.org/10.3189/172756506781828502, 2006.

Jeofry, H., Ross, N., Le Brocq, A., Graham, A. G. C., Li, J., Gogineni, P., Morlighem, M., Jordan, T., and Siegert, M. J.: Hard rock landforms generate 130 km ice shelf channels through water focusing in basal corrugations, Nature Communications, 8, 4576, https://doi.org/10.1038/s41467-018-06679-z, 2018.

Jourdain, N. C., Mathiot, P., Merino, N., Durand, G., Le Sommer, J., Spence, P., Dutrieux, P., and Madec, G.: Ocean circulation and sea-ice thinning induced by melting ice shelves in the Amundsen Sea, Journal of Geophysical Research: Oceans, 122, 2550–2573, https://doi.org/10.1002/2016JC012509, 2017.

Kovacs, A., Gow, A. J., and Morey, R. M.: The in-situ dielectric constant of polar firn revisited, Cold Regions Science and Technology, 23, 245 – 256, https://doi.org/10.1016/0165-232X(94)00016-Q, 1995.

Langley, K., von Deschwanden, A., Kohler, J., Sinisalo, A., Matsuoka, K., Hattermann, T., Humbert, A., Nøst, O., and Isaksson, E.: Complex network of channels beneath an Antarctic ice shelf, Geophysical Research Letters, 41, 1209–1215, https://doi.org/10.1002/2013GL058947, 2014.

Larour, E., Seroussi, H., Morlighem, M., and Rignot, E.: Continental scale, high order, high spatial resolution, ice sheet modeling using the Ice Sheet System Model (ISSM), Journal of Geophysical Research: Earth Surface, 117, F01 022, https://doi.org/10.1029/2011JF002140, 2012.

Le Brocq, A. M., Ross, N., Griggs, J. A., Bingham, R. G., Corr, H. F., Ferraccioli, F., Jenkins, A., Jordan, T. A., Payne, A. J., Rippin, D. M., et al.: Evidence from ice shelves for channelized meltwater flow beneath the Antarctic Ice Sheet, Nature Geoscience, 6, 945, https://doi.org/10.1038/ngeo1977, 2013.

Lee, E. H.: Elastic-plastic deformation at finite strains, Journal of Applied Mechanics, 36, 1–6, https://doi.org/10.1115/1.3564580, 1969.

Lindbäck, K., Moholdt, G., Nicholls, K. W., Hattermann, T., Pratap, B., Thamban, M., and Matsuoka, K.: Spatial and temporal variations in basal melting at Nivlisen ice shelf, East Antarctica, derived from phase-sensitive radars, The Cryosphere, 13, 2579–2595, https://doi.org/10.5194/tc-13-2579-2019, 2019.

MacAyeal, D. R.: Thermohaline circulation below the Ross Ice Shelf: A consequence of tidally induced vertical mixing and basal melting, Journal of Geophysical Research: Oceans, 89, 597–606, https://doi.org/https://doi.org/10.1029/JC089iC01p00597, 1984.

Marsh, O. J., Fricker, H. A., Siegfried, M. R., Christianson, K., Nicholls, K. W., Corr, H. F., and Catania, G.: High basal melting forming a channel at the grounding line of Ross Ice Shelf, Antarctica, Geophysical Research Letters, 43, 250–255, https://doi.org/10.1002/2015GL066612, 2016.

Martos, Y. M., Catalán, M., Jordan, T. A., Golynsky, A., Golynsky, D., Eagles, G., and Vaughan, D. G.: Heat Flux Distribution of Antarctica Unveiled, Geophysical Research Letters, 44, 11,417–11,426, https://doi.org/10.1002/2017GL075609, 2017.

Millgate, T., Holland, P. R., Jenkins, A., and Johnson, H. L.: The effect of basal channels on oceanic ice-shelf melting, Journal of Geophysical Research: Oceans, 118, 6951–6964, https://doi.org/10.1002/2013JC009402, 2013.

Morlighem, M.: MEaSUREs BedMachine Antarctica, Version 2. Boulder, Colorado USA. NASA National Snow and Ice Data Center Distributed Active Archive Center, Accessed 12 April 2021, https://doi.org/10.5067/E1QL9HFQ7A8M, 2020.

Morlighem, M., Rignot, E., Binder, T., Blankenship, D., Drews, R., Eagles, G., Eisen, O., Ferraccioli, F., Forsberg, R., Fretwell, P., Goel, V., Greenbaum, J. S., Gudmundsson, H., Guo, J., Helm, V., Hofstede, C., Howat, I., Humbert, A., Jokat, W., Karlsson, N. B., Lee, W. S.,

Matsuoka, K., Millan, R., Mouginot, J., Paden, J., Pattyn, F., Roberts, J., Rosier, S., Ruppel, A., Seroussi, H., Smith, E. C., Steinhage, D., Sun, B., Broeke, M. R. v. d., Ommen, T. D. v., Wessem, M. v., and Young, D. A.: Deep glacial troughs and stabilizing ridges unveiled beneath the margins of the Antarctic ice sheet, Nature Geoscience, 13, 132–137, https://doi.org/10.1038/s41561-019-0510-8, 2020.

865 Mouginot, J., Rignot, E., and Scheuchl, B.: MEaSUREs Phase-Based Antarctica Ice Velocity Map, Version 1. Boulder, Colorado USA. NASA National Snow and Ice Data Center Distributed Active Archive Center, Accessed 13 April 2021, https://doi.org/10.5067/PZ3NJ5RXRH10, 2019a.

Mouginot, J., Rignot, E., and Scheuchl, B.: Continent-Wide, Interferometric SAR Phase, Mapping of Antarctic Ice Velocity, Geophysical Research Letters, 46, 9710–9718, https://doi.org/10.1029/2019GL083826, 2019b.

870 Naughten, K. A., De Rydt, J., Rosier, S. H. R., Jenkins, A., Holland, P. R., and Ridley, J. K.: Two-timescale response of a large Antarctic ice shelf to climate change, Nature Communications, 12, 1991, https://doi.org/10.1038/s41467-021-22259-0, 2021.

Neff, P., Ghiba, I.-D., and Lankeit, J.: The exponentiated Hencky-logarithmic strain energy. Part I: constitutive issues and rank-one convexity, Journal of Elasticity, 121, 143–234, https://doi.org/10.1007/s10659-015-9524-7, 2015.

Nicholls, K. W.: Predicted reduction in basal melt rates of an Antarctic ice shelf in a warmer climate, Nature, 388, 460–462, 875 https://doi.org/10.1038/41302, 1997.

Nicholls, K. W.: The study of ice shelf-ocean interaction—techniques and recent results, Advances in Polar Science, 3, 222–230, https://doi.org/10.13679/j.advps.2018.3.00222, 2018.

Nicholls, K. W., Corr, H. F., Stewart, C. L., Lok, L. B., Brennan, P. V., and Vaughan, D. G.: A ground-based radar for measuring vertical strain rates and time-varying basal melt rates in ice sheets and shelves, Journal of Glaciology, 61, 1079–1087, 880 https://doi.org/10.3189/2015JoG15J073, 2015.

Pattyn, F.: A new three-dimensional higher-order thermomechanical ice sheet model: Basic sensitivity, ice stream development, and ice flow across subglacial lakes, J. Geophys. Res. Solid Earth, 108, https://doi.org/10.1029/2002JB002329, 2003.

Reeh, N., Mayer, C., Olesen, O. B., Christensen, E. L., and Thomsen, H. H.: Tidal movement of Nioghalvfjerdsfjorden glacier, northeast Greenland: observations and modelling, Annals of Glaciology, 31, 111–117, https://doi.org/10.3189/172756400781820408, 2000.

885 Rignot, E. and Steffen, K.: Channelized bottom melting and stability of floating ice shelves, Geophysical Research Letters, 35, https://doi.org/10.1029/2007GL031765, 2008.

Rizzoli, P., Martone, M., Gonzalez, C., Wecklich, C., Borla Tridon, D., Bräutigam, B., Bachmann, M., Schulze, D., Fritz, T., Huber, M., Wessel, B., Krieger, G., Zink, M., and Moreira, A.: Generation and performance assessment of the global TanDEM-X digital elevation model, ISPRS Journal of Photogrammetry and Remote Sensing, 132, 119–139, https://doi.org/10.1016/j.isprsjprs.2017.08.008, 2017.

890 Schultz, T.: Viskoelastische Modellierung der Dynamik eines Gletschers als Antwort auf basales Schmelzen und die Oberflächenmassenbilanz, Master thesis, 2017.

Sergienko, O.: Basal channels on ice shelves, Journal of Geophysical Research: Earth Surface, 118, 1342–1355, https://doi.org/10.1002/jgrf.20105, 2013.

Seroussi, H., Nakayama, Y., Larour, E., Menemenlis, D., Morlighem, M., Rignot, E., and Khazendar, A.: Continued retreat of 895 Thwaites Glacier, West Antarctica, controlled by bed topography and ocean circulation, Geophysical Research Letters, 44, 6191–6199, https://doi.org/10.1002/2017GL072910, 2017.

Smith, B. E., Fricker, H. A., Joughin, I. R., and Tulaczyk, S.: An inventory of active subglacial lakes in Antarctica detected by ICESat (2003–2008), Journal of Glaciology, 55, 573–595, https://doi.org/10.3189/002214309789470879, 2009.

Stanton, T., Shaw, W., Truffer, M., Corr, H., Peters, L., Riverman, K., Bindschadler, R., Holland, D., and Anandakrishnan, S.: Channelized ice melting in the ocean boundary layer beneath Pine Island Glacier, Antarctica, Science, 341, 1236–1239, https://doi.org/10.1126/science.1239373, 2013.

Stewart, C. L., Christoffersen, P., Nicholls, K. W., Williams, M. J., and Dowdeswell, J. A.: Basal melting of Ross Ice Shelf from solar heat absorption in an ice-front polynya, Nature Geoscience, 12, 435, https://doi.org/10.1038/s41561-019-0356-0, 2019.

Sun, S., Hattermann, T., Pattyn, F., Nicholls, K. W., Drews, R., and Berger, S.: Topographic shelf waves control seasonal melting near Antarctic ice shelf grounding lines, Geophysical Research Letters, 46, 9824–9832, 2019.

Timmermann, R. and Hellmer, H.: Southern Ocean warming and increased ice shelf basal melting in the twenty-first and twenty-second centuries based on coupled ice-ocean finite-element modelling, Ocean Dynamics, 63, https://doi.org/10.1007/s10236-013-0642-0, 2013.

van Wessem, J., Reijmer, C., Morlighem, M., Mouginot, J., Rignot, E., Medley, B., Joughin, I., Wouters, B., Depoorter, M., Bamber, J., et al.: Improved representation of East Antarctic surface mass balance in a regional atmospheric climate model, Journal of Glaciology, 60, 761–770, https://doi.org/10.3189/2014JoG14J051, 2014.

Vaňková, I., Nicholls, K. W., Corr, H. F., Makinson, K., and Brennan, P. V.: Observations of tidal melt and vertical strain at the Filchner-Ronne Ice Shelf, Antarctica, Journal of Geophysical Research: Earth Surface, 125, e2019JF005 280, https://doi.org/10.1029/2019JF005280, 2020.

Vaňková, I., Nicholls, K. W., and Corr, H. F. J.: The Nature of Ice Intermittently Accreted at the Base of Ronne Ice Shelf, Antarctica, Assessed Using Phase-Sensitive Radar, Journal of Geophysical Research: Oceans, 126, e2021JC017 290, https://doi.org/10.1029/2021JC017290, 2021.

Vaughan, D. G., Corr, H. F., Bindschadler, R. A., Dutrieux, P., Gudmundsson, G. H., Jenkins, A., Newman, T., Vornberger, P., and Wingham, D. J.: Subglacial melt channels and fracture in the floating part of Pine Island Glacier, Antarctica, Journal of Geophysical Research: Earth Surface, 117, https://doi.org/10.1029/2012JF002360, 2012.

Washam, P., Nicholls, K. W., Münchow, A., and Padman, L.: Summer surface melt thins Petermann Gletscher Ice Shelf by enhancing channelized basal melt, Journal of Glaciology, 65, 662–674, https://doi.org/10.1017/jog.2019.43, 2019.

Wearing, M. G., Stevens, L. A., Dutrieux, P., and Kingslake, J.: Ice-Shelf Basal Melt Channels Stabilized by Secondary Flow, Geophysical Research Letters, 48, e2021GL094 872, https://doi.org/10.1029/2021GL094872, 2021.

Xiao, H.: Hencky strain and Hencky model: extending history and ongoing tradition, Multidiscipline Modeling in Materials and Structures, 1, 1–52, https://doi.org/10.1163/1573611054455148, 2005.

Zeising, O. and Humbert, A.: Indication of high basal melting at the EastGRIP drill site on the Northeast Greenland Ice Stream, The Cryosphere, 15, 3119–3128, https://doi.org/10.5194/tc-15-3119-2021, 2021.

Zeising, O., Helm, V., Steinhage, D., and Humbert, A.: GNSS measurements at a basal melt channel of the southern Filchner Ice Shelf, Antarctica, https://doi.org/10.1594/PANGAEA.932441, 2021a.

Zeising, O., Steinhage, D., and Humbert, A.: Autonomous phase-sensitive radar (ApRES) measurements at a basal melt channel of the southern Filchner Ice Shelf, Antarctica between 2016/17 and 2017/18, https://doi.org/10.1594/PANGAEA.932413, 2021b.

Zeising, O., Steinhage, D., and Humbert, A.: Stake surface accumulation measurements at Filchnner Ice Shelf between December 2015/January 2016 and December 2016, https://doi.org/10.1594/PANGAEA.940252, 2021c.

Zeising, O., Steinhage, D., and Humbert, A.: Melt rates of 44 repeated phase-sensitive radar point measurements between December 2015/January 2016 and December 2016 at the Filchner Ice Shelf, Antarctica, https://doi.org/10.1594/PANGAEA.941400, 2022a.

Zeising, O., Steinhage, D., Nicholls, K. W., Corr, H. F. J., Stewart, C. L., and Humbert, A.: Basal melt of the southern Filchner Ice Shelf, Antarctica, The Cryosphere, 16, 1469–1482, https://doi.org/10.5194/tc-16-1469-2022, 2022b.